Available online at www.sciencedirect.com

ScienceDirect

journal homepage: www.elsevier.com/locate/he

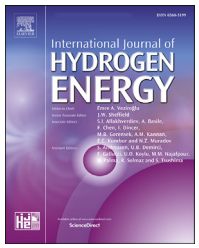

Decarbonisation potential of dimethyl ether/hydrogen mixtures in a flameless furnace: Reactive structures and pollutant emissions

Saurabh Sharma [a,b,*], *Matteo Savarese* [a,b], *Axel Coussement* [a,b], *Alessandro Parente* [a,b]

[a] *Université Libre de Bruxelles, École polytechnique de Bruxelles, Aero-Thermo-Mechanics Laboratory, Avenue F.D. Roosevelt 50, 1050, Brussels, Belgium*

[b] *Université Libre de Bruxelles and Vrije Universiteit Brussel, Brussels Institute for Thermal-Fluid Systems and Clean Energy (BRITE), Brussels, Belgium*

HIGHLIGHTS

- No visible flame structures for pure DME, DME/CH_4, but a flame appeared for DME/H_2.
- Single-digit NO for 100% DME with no other pollutants observed in flameless mode.
- Reactive structures revealed increased homogeneity with CH_4 addition.
- Reached zero pollutant levels at 50% CH_4 (vol.); however, high CO at 60% CH_4 (vol.)
- Increased NO at higher H_2 with 50% H_2 (vol.) as the optimum level for H_2 addition.

ARTICLE INFO

Article history:
Received 8 July 2022
Received in revised form
6 October 2022
Accepted 12 October 2022
Available online 3 November 2022

Keywords:
MILD
Distributed combustion
Flameless combustion
Dimethyl ether
Emissions
Chemiluminescence

ABSTRACT

This article sheds light on the combustion characteristics of dimethyl ether and its mixtures with methane/hydrogen under flameless conditions at different equivalence ratios. It was found that combustion of 100% dimethyl ether in flameless conditions minimises the NO formation, keeping it less than 10 ppm with no CO or unburned hydrocarbons. Progressive addition of methane was found to reduce the NO, reaching up to zero value at 50% methane in molar fraction along with a marginal CO_2 reduction. However, large amounts of CO were found for higher methane levels, greater than 60% CH_4 in molar fraction. Reactive structures based on OH* chemiluminescence revealed that adding methane results in increased ignition delay times and, consequently, a more distributed reaction zone characterised by reduced temperature gradients. No visible flame was observed for pure dimethyl ether as well as dimethyl ether/methane mixtures. Furthermore, a more intense and narrower reaction zone, characterised by the presence of a visible flame, was formed upon hydrogen addition. Adding hydrogen by 50% in molar fraction did not cause a noticeable rise in NO levels; however, CO_2 was lowered by about 18%. Further addition of hydrogen resulted in increased peak temperatures of about 1700 K and higher NO emissions of about 50 ppm. Additionally, a skeletal Chemical Reactor Network was built and simulated with the commercial software CHEMKIN Pro to investigate the effect of the different mixtures and operating conditions on NO formation from a chemical point of

* *Corresponding author*. Université Libre de Bruxelles, École polytechnique de Bruxelles, Aero-Thermo-Mechanics Laboratory, Avenue F.D. Roosevelt 50, 1050, Brussels, Belgium.
E-mail address: saurabh.sharma@ulb.be (S. Sharma).

https://doi.org/10.1016/j.ijhydene.2022.10.104

view. N_2O pathway was observed to be the root source of NO emissions for pure DME and DME/CH_4 mixtures, however; the thermal pathway became gradually more important as hydrogen concentration was increased in the mixture.

Introduction

Renewable synthetic fuels have emerged as a potential future fuel choice in recent times due to faster depleting fossil fuels, ever stringent emission norms, and uncertain political scenarios. Dimethyl ether (CH_3OCH_3) is one of such promising synthetic fuels due to benefits such as high combustion efficiency and low pollutant emissions (CO, HC, SO_2 etc.) [1]. At ambient conditions, Dimethyl ether (DME) is a gas; however, it can be stored in liquid form under slightly pressurised conditions (about 5 bar). DME can be produced from biomass [2,3] and existing fossil fuels such as coal and natural gas [3]. It is also used as a hydrogen carrier and can be easily reformed back to hydrogen at low temperatures [3]. Due to the absence of a carbon-carbon bond and an oxygen content of about 35%, the particulate matter emissions are also very low [4–6]. DME is colourless, non-toxic, non-carcinogenic, and highly flammable, and it generates one of the lowest levels of the well-to-wheel greenhouse gas emissions [3]. DME has the potential to reduce greenhouse gas emissions by up to 85% if it is produced from renewable sources [7]. Such characteristics make it a potential alternative to the petroleum fuels and natural gas [8,9]. DME is characterised by high fuel reactivity and low ignition delay times [10]. Therefore, it has been used as an ignition enhancer to improve the reactivity of methane-containing fuel mixtures [10–12]. It was reported in these works that a small DME addition can significantly lower the ignition delay times while increasing the laminar flame speed.

Primarily, DME has been investigated as a potential alternative fuel in the internal combustion engines [13–18] and as a domestic cooking gas [19–24]. DME has also been studied for gas turbines applications [25–28] and power generation [29,30]. These studies demonstrated that replacing conventional fuels with DME improves combustion characteristics with considerably low NO_x and CO emissions. Investigations on the usage of DME in industrial furnaces are however limited [31–33]. Chen et al. [31] investigated the characteristics of DME and propane in a ceramic kiln furnace by varying the oxygen levels in the air between 10% and 90%. They reported that for similar input conditions of thermal power and oxygen content, DME produces lower temperatures compared to propane along with no soot, no unburnt fuel, low CO, and low NO_x emissions [31]. Reactive structures of premixed DME-air flame were investigated in a cylindrical boiler furnace for two thermal loads (130 kW and 270 kW) and a range of excess air ratios (1.05, 1.15, 1.30, 1.45, 1.60) [32]. Three different zones were identified in this furnace: a high-temperature flame core area, followed by two different recirculation zones with relatively low temperatures, formed between the flame zone and furnace walls. At higher excess air ratios, the reaction zone was reported to be shortened in length and shrunk in volume, mainly due to the increased mean reaction rate. Moreover, the reaction zone was observed to be broadened and elongated at a high load for a fixed air excess ratio. Indeed, at a fixed air ratio, the mean reaction rate was identical for both low and high loads and in such cases, more fuel-air mixture at high load results in a large reaction zone [32]. Emissions of CO_2 were lower at increased air excess; however, they appeared to be independent of thermal load. Kang et al. [33] studied the characteristics of the same DME-fired boiler furnace [32] in terms of CO and NO_x emissions for variable thermal loads and air excess ratios. They identified the NO_x formation from a thermal pathway in the high temperature (1800 K) flame area and from an intermediate N_2O pathway in the relatively low temperature (1000–1600 K) recirculation zone. However, most of the NO_x was produced from the thermal pathway. Both NO_x and CO were lower at higher air excess ratios. NO_x did not respond much to the variable thermal load; however, CO increased with an increase in load. Kang et al. [33] were able to reduce the NO_x and CO up to 56 ppm and 6.2 ppm, respectively, at an air excess of 1.2, thereby proving the clean combustion capabilities of DME. In another study, Kang et al. [34] investigated DME-air jet diffusion flames in a coaxial burner representing the boiler furnace case. They reported that most of the NO_x in DME air diffusion flame was formed via thermal and prompt pathways due to the presence of a high-temperature flame zone [34].

Apart from DME, methane and hydrogen also fall in the category of alternative fuels which are being investigated extensively. Both methane and hydrogen can be used to control the ignition time and to broaden the operational range of DME-fired combustion systems [35]. Therefore, study of DME/CH_4 and DME/H_2 mixtures in different combustion system is important. Kang et al. [36] investigated the effect of H_2 addition on the flame structure and pollutant emissions of DME jet diffusion flame in a coaxial burner while maintaining the fuel jet velocity. They observed significant changes in the reaction zone size, temperature, and species concentration as the H_2 mole fraction in the fuel mixture exceeded 60%. The length and width of the reaction zone decreased almost linearly, however; the length reduced faster for H_2 > 60%. They proposed that the optimal level of H_2 dilution into DME was 60% by vol. in practical engineering. DME/CH_4 jet diffusion flames were investigated numerically and experimentally by Kang et al. [37] in the same coaxial burner [36] to analyse soot formation and NO_x emissions. They reported significant soot reduction even with smaller DME addition (20% vol.); however, at higher DME content, soot reduced rather slowly. NO_x formation in DME/CH_4 flames was simulated considering the thermal, prompt, NNH-, and N_2O- intermediate pathways. Thermal and prompt dominated the NO_x formation while

NNH and N_2O routes contributed marginally. Thermal NO_x increased with DME addition due to higher availability of OH while prompt decreased due to reduced availability of CH, a major prompt precursor. In summary, the NO_x first decreased, reaching a minimum at 60% DME and then increased. Bhattacharya et al. [38] numerically analysed the effect of DME blending into CH_4 on NO emissions in a counterflow diffusion flame. It was observed that the thermal route was the dominant source of NO production for all fuel blends. They found that DME addition to CH_4 results in lower NO levels because of a) relatively lower flame temperature thereby reducing the thermal NO and b) consumption of NO due to increased availability of CH_3 radicals. Some kinetic modelling studies highlighted the importance of DME as an ignition promotor [10,11,35,39]. Chen et al. [11] studied the potential of DME as an ignition enhancer for high-temperature homogeneous ignition of methane-air mixtures and found that even a small amount of DME addition could lead to a significant reduction in ignition delay times. It was attributed to the large availability of CH_3 and CH_2O radicals due to DME addition. The chain propagation reaction based on CH_3 and CH_2O then replaced the slow chain reaction including CH_3 and O_2 in the case of pure methane. Tang et al. [10] studied the ignition delay times of DME/CH_4 mixtures in shock-tube experiments over a wide range of temperatures. They observed a significant decrease in ignition delay with increasing DME addition, however; the effect weakened after a 20% DME blending ratio. Wang et al. [35] studied numerically the homogeneous ignition process for different DME/CH_4 and DME/H_2 mixtures aimed at the development of a more realistic DME-based combustion engine. They simulated a constant volume adiabatic homogeneous ignition process at 10 bar and 900 K/1400 K for different DME/CH_4 and DME/H_2 mixtures. It was found that at low temperatures, the ignition delay time increased with the addition of both CH_4 and H_2. However, at high temperatures, H_2 addition led to reduced ignition delay times due to the rapid production of highly active radicals. Moreover, maximum NO was marginally affected by CH_4 or H_2 addition because NO was mainly produced from a temperature-sensitive thermal pathway. Pan et al. [39] investigated the ignition delay times of DME/H_2 mixtures in a shock tube. They found that for DME/H_2 mixtures, the ignition is controlled by DME chemistry; if the H_2 mole fraction is less than 80% and it becomes both DME and H_2 controlled for H_2 levels between 80% and 98%. Moreover, for the H_2 mole fraction greater than 98%, the ignition was entirely controlled by H_2 chemistry. It was found that H_2 addition could promote the DME ignition, however, the ignition delay time dependence on temperature became complex for H_2 greater than 98%. In the literature, there are also studies on the laminar burning velocities of the DME/CH_4/H_2 mixtures [40–42]. Lowry et al. [41] investigated the effect of DME addition to CH_4 on the laminar burning velocity at elevated pressures. The flame speed of the mixtures was observed to be increased almost linearly with DME addition. Yu et al. [42] measured the laminar flame speed of DME/H_2 mixtures at different temperatures and H_2 blending ratios in a constant volume bomb. They found that laminar flame speed increases with increasing H_2 content in the mixture. Kinetic effects dominated the thermal and diffusive effects in enhancing the flame speed due to H_2 addition. Liu et al. [40] also analysed the chemical effect of H_2 addition on DME/H_2 pre-mixed flames. They concluded that dominating chemical effect of H_2 addition results in an increased mole fraction of H, O, and OH radicals which enhance the combustion process.

The vision of the combustion industry for future systems is to have a fuel-flexible, efficient, highly reliable, and environment-friendly combustion system [43]. The requirement is to limit the NO_x emissions to under 10 ppm as a short-term goal and 2 ppm in the coming decades [43]. Flameless combustion [44] has gained the attention of combustion scientists due to its ability to deliver on all aspects mentioned above. The most significant advantage of this technology is fuel flexibility and ultra-low NO_x emissions [44]. In a flameless regime, combustion reaction occurs in a highly diluted and heated environment, achieved by excessive exhaust gas recirculation. Hence, locally, the oxygen concentration is well below the atmospheric level, thus preventing the instantaneous ignition of the reactant mixture. Rather, a slow combustion reaction starts as the temperature of the reactant mixture exceeds the auto-ignition temperature. The reactions then happen in a distributed manner over a large volume, and it is characterised by a uniform temperature profile, ultra-low pollutant emissions, and reduced pressure fluctuations. The flameless regime demonstrates superior flame stability due to high preheating levels of reactants [44,45]. Over the years, the definition of flameless technology has undergone several changes based on the concept of reactant dilution. It is also known as HiTAC [46], MILD (moderate or intense low dilution oxygen) [45], and Colorless Distributed Combustion (CDC) [47].

In the previous two decades, flameless combustion has been widely explored with conventional fuels such as natural gas [44,48–51], liquified petroleum gas [50,52,53], and kerosene [54,55]. However, the demand to significantly reduce greenhouse gas emissions by 2050 enforces the substantial inclusion of renewable synthetic fuels in industrial heating applications. Flameless combustion has the potential to burn these non-conventional fuels due to its enhanced stability, achieved through dilution and preheating of reactants. Synthetic fuels have been investigated in flameless combustion systems by many researchers [56–64]. Derudi et al. [58] studied the combustion behaviour of coke oven gas, a hydrogen-containing byproduct, in a laboratory-scale flameless burner. They concluded that increased dilution levels are required to sustain flameless combustion for hydrogen-containing fuels. Huang et al. [60] presented similar findings for synthetic gas, where enhanced recirculation and air preheating helped attain flameless conditions. Colorado et al. [57] investigated biogas and natural gas in a flameless furnace. They reported relatively lower temperatures for biogas than natural gas due to the presence of CO_2 in biogas, which exhibits better radiation characteristics. Hosseini et al. [59,65] compared biogas flameless combustion with conventional methane combustion in terms of temperatures and efficiency. Due to the presence of CO_2, Biogas produced relatively low and uniform temperatures compared to conventional methane combustion. Ardila et al. [56] studied the effect of hydrogen addition by up to 60% vol. on NO_x emissions and burner stability under the sub-atmospheric condition of 0.85 bar. They reported that NO_x was significantly affected at a lower level of H_2 addition.

However, it stopped increasing beyond a certain H_2 dilution level due to a lower C/H ratio. In flameless conditions, prompt NO is one of the significant contributors to NO_x and is directly proportional to the C/H ratio. H_2 addition resulted in a decrease in CO_2 levels; moreover, it helped improve the stability due to better thermal diffusivity. Zhao et al. [61] investigated the effect of hydrogen addition to pipeline natural gas on temperature, emissions, and burner stability in a central air heating residential furnace. It was observed that hydrogen addition doesn't alter the ignition time much; however, flashbacks started occurring at 45% hydrogen addition.

Ferrarotti et al. [66] studied the flameless combustion of CH_4–H_2 blends in a semi-industrial furnace. It was found that adding hydrogen to methane causes a reduction in ignition delay and increases the reactivity of the system, which was confirmed based on OH* measurements. A visible flame started appearing from a threshold H_2 content of 25% vol. However, the conditions for flameless operation [66] were still met. Adding H_2 led to a rise in NO levels; however, increasing the air injection velocity (by reducing the air injection diameter) helped lower the NO. Sorrentino et al. [67] explored ammonia flameless combustion in a cyclonic burner. The cyclonic combustion chamber could sustain the flameless combustion even with pure ammonia under highly preheated and diluted conditions. NO_x levels, the major harmful pollutant in ammonia combustion, were measured below 100 ppm. They found that burner operational temperature below 1300 K should be avoided to reduce the risk of flame extinction.

A series of investigations have been carried out on fuel mixtures such as hydrogen, syngas, biogas, and ammonia in both lab-scale and industrial flameless systems. However, a few reported the combustion characteristics of dimethyl ether and that only in lab-scale systems [68,69]. DME is a clean alternative fuel for soot, sulfur, and hydrocarbons emissions; however, the NO_x is primarily formed through thermal pathways, mainly due to high adiabatic flame temperatures. Given the potential of flameless technology in terms of NO_x emissions and fuel flexibility, it is vital to investigate how DME respond to the flameless regime. In addition, it is also important to study the DME/CH_4 mixtures as DME suffers from low ignition delay times, which is not a desirable characteristic in a flameless regime. Hence burning methane together with DME can help create an ideal environment for flameless combustion, offering decarbonisation solutions in the industry. Moreover, the addition of hydrogen to DME can result in a reduced level of carbon footprint. Combustion of DME/H_2 mixture can alleviate the several drawbacks of burning pure hydrogen, e.g., a) it can reduce the peak temperatures and thereby reduce the high NO_x levels, b) it can improve the life of furnace refractory material by avoiding hot spots. Kang et al. [68] studied DME flameless combustion in a lab-scale coaxial jet burner for a range of co-flow temperatures and oxygen concentrations. They reported relatively uniform temperature profiles at low oxygen levels and high co-flow temperatures, indicating an improved combustion process in a flameless regime. The measured CO was lower than coal-flameless combustion; however, it was higher than syngas-flameless combustion. NO_x reduced significantly compared to conventional DME combustion. Based on chemical kinetics, they concluded that NO_x was mainly produced from NNH, N_2O intermediate, and prompt pathways in the flameless regime, with NNH accounting for almost half of total NO_x emissions. In contrast, thermal NO_x was insignificant [68].

To the best of the author's knowledge, no study has focused to date on the characteristics of dimethyl ether in a flameless furnace at a semi-industrial scale. The objective of the present work is to test the feasibility of DME in a flameless capable furnace. This study also sheds light on the effect of methane and hydrogen addition to DME on reactive structures and pollutant emissions. For different fuel mixtures, measurements were carried out for in-furnace temperatures, OH* chemiluminescence, and exhaust pollutant species emissions. Initially, experimental details along with measurement methods and different uncertainties are presented. Later, analyses for pure DME, DME/CH_4 and DME/H_2 mixtures are presented in terms of reactive structures and pollutant emissions. The last section presents a detailed kinetic analysis of different fuel mixtures.

Experimental details

The experimental set-up consists of a reverse flow semi-industrial furnace equipped with a recuperative flame/FLOX® burner. The schematic line diagram of the integrated furnace-burner assembly is shown in Fig. 1. The furnace is a cubical chamber (1100 mm × 1100 mm x 1100 mm) made of stainless steel and is insulated with a 200 mm thick layer of high temperature (~1300 °C) ceramic fibre blanket. The insulation is aimed to reduce heat loss to help establish flameless combustion conditions. Therefore, the observable internal section of the furnace is of size 700 mm × 700 mm x 700 mm. The furnace is fired using a 20 kW capacity recuperative commercial flame/FLOX® burner (REKUMAT M150) of WS make. This burner is mounted at the bottom of the furnace, as shown in Fig. 1 and integrated with a metallic finned heat exchanger. This is aimed at preheating the incoming combustion air using the heat extracted from the outgoing exhaust gases. On the right side of Fig. 1, the air/fuel injection strategy is explained. It consists of a central fuel injection nozzle and a coaxial channel for air injection. The diameter of the fuel injection nozzle and air injection nozzle is 8 mm and 16 mm, respectively. The air injection diameter is variable (16, 20, and 25 mm); however, for the present work, a 16 mm air injector was chosen based on emission and temperature measurements for all three injectors. The 16 mm injector resulted in the lowest NO levels among all three injectors. A detailed justification for the choice of air injector is provided in the supplementary section.

Provisions are made to run the furnace in flame and flameless modes. Indeed, this burner cannot directly start in flameless mode due to low initial furnace temperatures (room temperature). The burner is switched on in flame mode for heating the furnace, where air and fuel are injected close to each other in partially premixed mode, and a stable flame is generated at the burner exit. The furnace is allowed to heat up in flame mode until the lowest possible temperature (mentioned as exhaust temperature in Fig. 1) in the furnace reaches the autoignition temperature of the fuel/air mixture. Then the burner is switched into flameless mode by changing the fuel injection to the central nozzle and the air from the coaxial

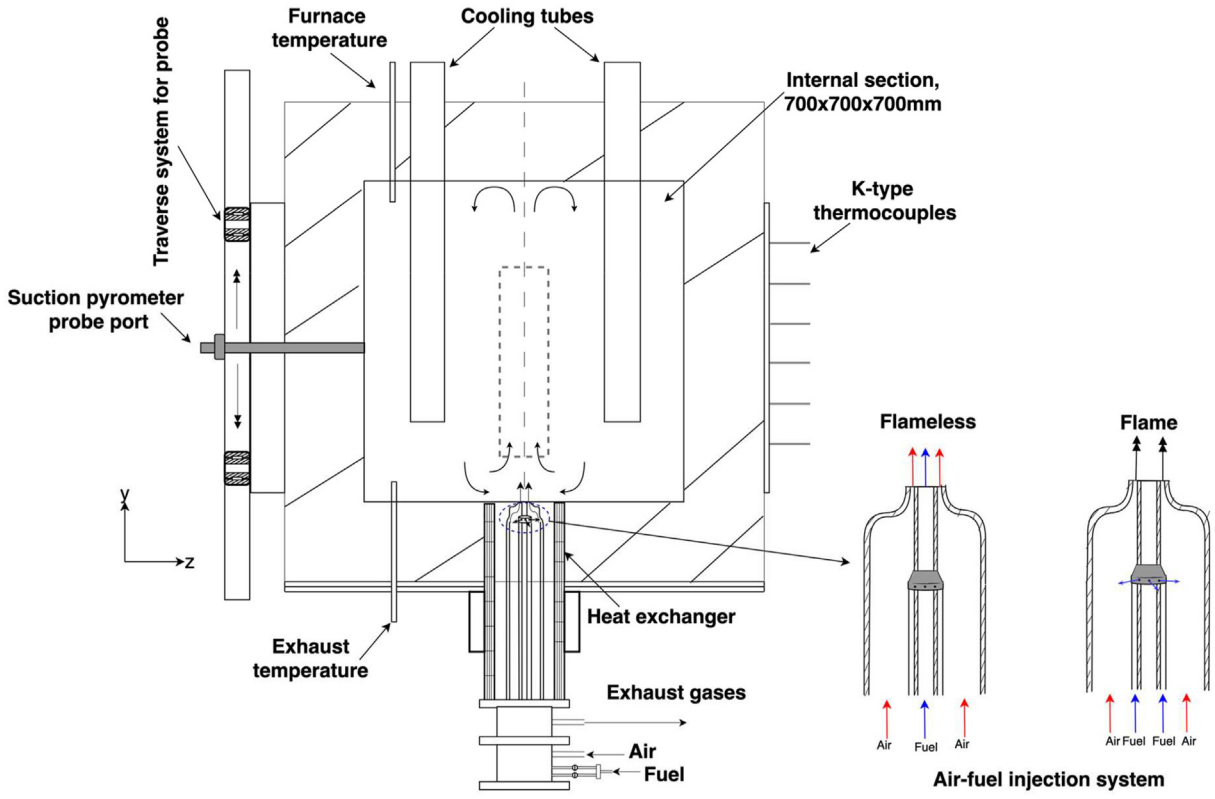

Fig. 1 – Schematic of the cross-section of flameless furnace.

channel, as shown in Fig. 1. Separately injected fuel and air are then mixed with recirculated exhaust gases, and flameless combustion is achieved.

As shown in Fig. 1, the furnace is equipped with an air cooling system at the top. It consists of four cooling pipes of 80 mm inner diameter and a length of 630 mm protruding inside the furnace. This arrangement facilitates the furnace operation at variable thermal loads by changing the mass flow of cooling air. Measurement openings are provided on each of the four vertical walls of the furnace. One opening is equipped with a 110 mm × 450 mm quartz window for optical measurements such as OH* and CH* chemiluminescence. The quartz panels (GE 124) have high thermal stability and transmissivity (~93%) in the 200–2000 nm wavelength range, thus enabling chemiluminescence measurement. Other openings host the temperature probe and various ports for thermocouples to monitor the wall temperatures. Fig. 2 shows the air/fuel supply system to the furnace. Two separate blowers supply combustion and cooling air. For flow control of fuel and air, Brooks makes mass flow controllers (SLA-585XX) are used. A static mixer is used to produce a uniform fuel mixture. A natural gas feeding system is also provided at 30 mbar via a three-way valve. A heating line is connected between furnace exhaust and gas analyser for emission measurement. Various high purity gas bottles are used as span gas for the analyser to calibrate the instrument. Also, high purity N_2 and synthetic air are used as zero gas. The analyser is calibrated every time before starting the experimental campaign with the help of high purity span gases. A metal grid houses bottles of fuels (CH_4, H_2, and DME), with DME bottles being wrapped in a heating blanket to avoid freezing in extremely cold conditions.

Measurement methods

This experimental work focuses on the i) measurement of temperature using a probe, ii) measurement of chemiluminescence using an (Intensified charge-coupled device) ICCD camera, and iii) measurement of pollutants using a (Fourier transform infrared spectroscopy) FTIR gas analyser.

Three types of thermocouples, namely, B-type, K-type, and N-type, were used to monitor various temperature levels of the furnace. One of the other three openings on the furnace hosts a semi-automatic system for the movement of the temperature probe. It allows the two-dimensional movement of the temperature probe (a suction pyrometer) at various locations inside the furnace with great accuracy. The system consists of different roller bearings, traverse mechanisms, gaskets, and a rope system to move the assembly. B-type thermocouple (~10 s response time) of 0.5 mm wire diameter (Platinum Rhodium 30%/Platinum Rhodium 6%), placed in an air-cooled suction pyrometer, was used to measure the in-furnace temperatures. Inside the suction pyrometer, the thermocouple is protected by two concentric alumina tubes to avoid the radiation heat exchange with the furnace walls. Details of the suction pyrometer assembly can be found in the previous work of the same research group [70]. This design ensures a powerful suction of hot gases such that the majority of the heat transfer to the thermocouple tip happens via convection. Thus, corrections due to radiation heat loss are avoided, and the measured temperature can be considered the actual gas temperature. On the second opening, six equally spaced K-type thermocouples (Nickel–Chromium/Nickel-Alumel) were flushed against the insulation to monitor

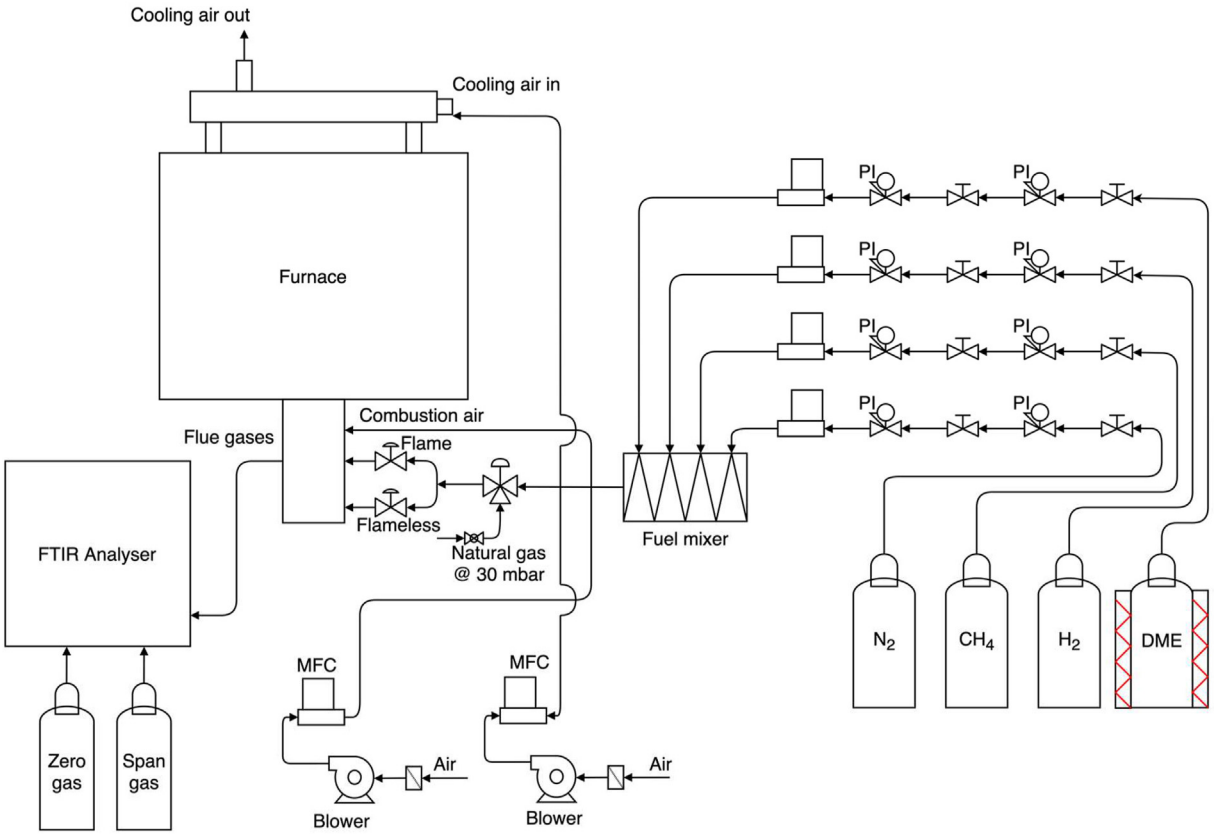

Fig. 2 – Schematic of piping and instrumentation diagram of the flameless test bench.

the inner wall temperatures at different axial locations. The third opening was kept closed for the present experimental campaign. Other K-type thermocouples monitor temperatures of the outer window, fuel, cooling air at the inlet/outlet, combustion air, and exhaust gases after the heat exchanger. A shielded N-type thermocouple (Nicrosil/Nisil) was used to measure the temperature of exhaust gases (just before the heat exchanger, as shown in Fig. 1). All thermocouples generate differential voltage signals, continuously sampled at 10 Hz and converted to units of temperature using a data acquisition system of National-Instrument make.

Chemiluminescence of OH* was measured to study different fuel mixtures' flame characteristics. An ICCD camera (16 bit - 1392x1040 pixels) of LaVison made together with a UV lens (78 mm f/3.8) was used to record the images. OH* was collected using an interferential filter; 310 ± 10 nm. The maximum acquisition frequency of the camera is 17 Hz. An automatic three-dimensional traverse system, driven by stepper motors, facilitates the movement of the camera to capture the images at various positions. The first and last accessible positions on the burner symmetry plane are 40 mm and 500 mm, respectively, from the exit plane of the burner. A total of 500 images were recorded for each condition, and the average is presented after subtracting the noise, which corresponds to the state of extinguished flame.

Pollutants such as CO, NO, and NO_2, along with major combustion products (CO_2 and H_2O), were measured using a heavy-duty emission analyser (HORIBA MEXA-ONE-FT). A heated sampling line connects the exhaust of the furnace and the analyser to avoid condensation. The analyser operates on the FTIR spectroscopy principle. A paramagnetic sensor measures the oxygen concentration after water is condensed from the exhaust gases, as O_2 is transparent to infrared.

Error analysis

In this section, uncertainties in fuel/airflow measurement, various temperatures, gaseous emissions, and equivalence ratios are calculated. Uncertainties in measurable variables, which in this study are, temperature and gaseous emissions, are considered due to instrument error (U_{instru}) and measurement error ($U_{measure}$). The manufacturer usually provides instrument errors, while measurement errors are calculated based on repeatability. The total error ($U_{\dot{n}}$) in an independent variable considering the 95% probability interval can then be expressed as:

$$U_{\dot{n}} = 1.96 * \sqrt{U_{instru}^2 + U_{measure}^2}$$

$U_{measure}$ is estimated based on the standard deviation (σ) of the measurement quantity and the total number of measurements (N) as follows:

$$U_{measure} = \sigma \Big/ \sqrt{N}$$

For in-furnace temperatures, a type B thermocouple is used, and the uncertainty provided by the manufacturer (U_{instru}) is ± 0.5% of the reading. During the test campaign, the

maximum uncertainty associated with measurement ($U_{measure}$) has been found as 1.5 K. Since the maximum recorded temperature is 1695 K. Therefore, the maximum average uncertainty in measured temperature is ±17 K. For K-type thermocouples used to measure the wall temperature, the uncertainty is 2.2 °C or 0.75% of the reading, whichever is maximum.

For the pollutant emissions, the instrument error for different species is calculated based on zero noise, linearity, and interference provided by the manufacturer. Table 1 shows the summary of different instrument uncertainties for each species. Details are presented only for the measurement ranges used in the present work.

Based on the information provided by the manufacturer, the instrument error of the gas analyser is calculated as:

$$U_{instru} = \sqrt{\left(\frac{U_{zero}}{\sqrt{3}}\right)^2 + \left(\frac{U_{linear}}{\sqrt{3}}\right)^2 + \left(\frac{U_{inter}}{\sqrt{3}}\right)^2}$$

After considering the maximum uncertainty in the measurement, the maximum total uncertainty for different species is as follows: CO (12 ppm), NO_low (3 ppm), NO_high (10 ppm), CO_2 (0.2% vol), O_2 (0.31% vol), and H_2O (0.24% vol).

Uncertainty in fuel and airflow rates are calculated based on the instrument error (U_{instru}) and error associated with the purity of gases (U_{pure}). For the present work, Brooks make MFCs (SLA-585XX) are used to control the flow of fuel and air, and the uncertainty associated with them is due to accuracy, repeatability, temperature drift, and pressure drift, as shown below:

$$U_{instru} = \sqrt{\left(\frac{U_{linear}}{\sqrt{3}}\right)^2 + \left(\frac{U_{repeat}}{\sqrt{3}}\right)^2 + \left(\frac{U_{drift,Temperature}}{\sqrt{3}}\right)^2}$$

Details regarding the values associated with these uncertainties are shown in Table 2.

For fuels, the uncertainty due to the purity is calculated based on the purity of the fuel gases. For the present work, the purity of different fuel gases is as follows: 99.5% for CH_4, 99.9% for H_2, and 99.99% for CH_3OCH_3. However, uncertainty in the purity of the combustion and cooling air is calculated after considering the uncertainties in the dry air composition and the moisture content [66]. The total uncertainty is calculated as shown in the equation below. Table 3 presents the total uncertainties in fuel and air mass flow rates after considering the 95% probability.

Table 1 – Summary of uncertainties in zero noise, linearity, and interference for different components.

Measurement species		Zero noise (% of full scale), U_{zero}	Linearity (% of full scale), U_{linear}	Interference (% of full scale), U_{inter}
CO	200 ppm	1	± 1	± 1
CO	1000 ppm	1	± 1	± 1
NO_low	200 ppm	2	± 1	± 1
NO_high	1000 ppm	1	± 1	± 1
CO_2	20% vol	1	± 1	± 1
O_2	25% vol	1.5	± 0.2	± 1.5
H_2O	24% vol	1	–	± 1

Table 2 – Details of the different uncertainties in Brooks SLA-585XX MFCs. SP refers to set point, and FS refers to full scale.

Source of uncertainty	Uncertainty value
Linearity	±0.9% SP
Linearity	±0.18% FS**
Repeatability	±0.2% FS
Temperature zero drift	±0.05% FS/K
Temperature span drift	±0.05% FS/K

*Drift in temperature is calculated based on both zero drift and span drift.
**if SP<20% FS.

$$U_{\dot{n}} = 1.96 * \sqrt{U_{instru}^2 + U_{pure}^2}$$

Test conditions

For the present work, a renewable fuel, dimethyl ether (CH_3OCH_3), was tested along with its mixtures with methane and hydrogen in a semi-industrial flameless furnace. This study investigates the potential of dimethyl ether and its mixtures in a flameless combustion regime in terms of pollutant emissions. Table 4 shows the different test conditions in terms of fuel mixture composition and equivalence ratio. Input thermal power (P_{th}) was kept constant at 15 kW for all conditions, and a 16 mm air injector was used. For all operating conditions, the cooling power (P_{cool}) of 6.5 kW was extracted with the help of a cooling air system to ensure an exhaust gas temperature of more than 1223 K before entering the heat exchanger. It is to be noted that since input power is kept constant, the fuel injection velocity (v_{fuel}) varies for different fuel mixtures (refer to Table 4). However, fuel velocity is one order of magnitude lower than the air injection velocity.

It is to be noted that inlet velocities for fuel and air are calculated based on their corresponding inlet temperatures. These temperatures could not be measured directly due to hardware limits, and they are calculated following the energy balance on the furnace. As shown in the air-fuel injection system of Fig. 1, unlike the air injection, the fuel lance is not preheated directly from the heat exchanger. The fuel lance is surrounded by the high-temperature combustion air and is heated indirectly. The energy balance shows that the fuel preheating is around 50 K, so the fuel inlet temperature is about 340K. Considering the ratio of air-fuel flow rates, it can be assumed that fuel preheating has a marginal effect on furnace performance. Air inlet temperatures are calculated following the energy balance on the heat exchanger, and their details are shown in Table 5.

Initially, the burner is turned on in normal flame mode with methane to heat the furnace. The heating period with methane is about 2 h after that the actual fuel composition is supplied, consisting of DME/CH_4/H_2. Once the minimum furnace temperature reaches sufficiently high values (around 1100 K), the burner is switched to flameless mode and allowed to reach steady-state flameless conditions. The average total time to reach a steady condition is about 4 h. A short description is used to represent the fuel composition for the following

Table 3 – Calculated uncertainties for different fuel and air mass flow rates at equivalence ratio, $\phi = 0.8$.

Case	Fuel flow rate, Nm^3/h	Uncertainty in fuel flow, U_{fuel} (%)	Combustion air flow rate, Nm^3/h	Uncertainty in combustion air flow, U_{air} (%)	Cooling air flow rate, Nm^3/h	Uncertainty in cooling air flow, U_{cool} (%)
D100M0	0.91	1.22	16.27	1.47	25.50	1.45
D70M30	1.03	1.53	16.61	1.46	25.50	1.45
D50M50	1.14	1.33	16.90	1.45	25.50	1.45
D40M60	1.20	1.27	17.07	1.45	25.50	1.45
D25M75	1.30	1.28	17.36	1.44	25.50	1.45
D50H50	1.52	1.83	16.06	1.48	25.50	1.45
D25H75	2.36	1.31	15.78	1.49	25.50	1.45

Uncertainty in the equivalence ratio is calculated based on the RSS method [71], and maximum uncertainties in the equivalence ratios of $\phi = 0.8$, 0.9, and 1 are calculated as 2.2% ($\phi = 0.8 \pm 0.021$), 2.5 ($\phi = 0.9 \pm 0.025$), and 2.8 ($\phi = 1 \pm 0.028$) respectively.

sections. D100 represents pure dimethyl ether. DxMy represents x % (vol.) of dimethyl ether and y % (vol.) of methane. Similarly, DxHy represents x % (vol.) of dimethyl ether and y % (vol.) of hydrogen.

Energy balance

In this section, a global heat balance is presented to analyse the performance of the furnace. This is also necessary to predict the values of various temperatures, which are important but cannot be measured directly due to the hardware limits of the furnace. These operating parameters are air and fuel inlet temperature, and for the present work, they are calculated following the energy balance. Here P_{th} is the power generated by the combustion. P_{cool} is the power taken out by the cooling system installed on the top of the furnace, and it is calculated based on mass flow rates-temperatures of air entering and leaving the cooling tubes. P_{wall} is the total heat loss through the furnace walls. It is calculated based on the measured wall temperatures by considering the heat loss from vertical and horizontal walls through radiation and natural convection. P_{rad} represents the energy loss through the quartz window, calculated based on the radiation energy emitted by the furnace insulation walls. In the end, P_{exh} is energy loss associated with the hot exhaust gases. It is calculated based on temperatures and mass flow rates of exhaust gases entering and leaving the heat exchanger. ΔP accounts for other losses not considered here. It is to be noted here that sensible enthalpies of fuel and air are neglected as they account for less than 1% of the total power. Table 5 presents the energy balance for D100, D25M75, and D25H75. The process efficiency (η_P) is also calculated by considering cooling power and radiation heat loss through the window. It is defined as $(P_{cool} + P_{rad})/(P_{th})$. The calculated values of η_P are 62.53%, 63.07%, and 62.80% for the cases of D100, D25M75, and D25H75, respectively.

Table 4 – Details of different operating conditions used for the experimental tests.

Test case	P_{th} [kW]	P_{cool} [kW]	ϕ	DME (vol%)	CH_4 (vol%)	H_2 (vol%)	v_{fuel} (m/s)
T1	15	6.5	0.8–1	100	–	–	6.27
T2	15	6.5	0.8–1	70	30	–	7.24
T3	15	6.5	0.8–1	50	50	–	7.96
T4	15	6.5	0.8–1	40	60	–	8.42
T5	15	6.5	0.8–1	25	75	–	9.13
T6	15	6.5	0.8–1	50	–	50	10.80
T7	15	6.5	0.8–1	25	–	75	16.51

Evaluation of MILD criterion

Finally, the MILD criterion was evaluated for all fuel mixtures following the approach provided by Cavaliere et al. [45], according to which a regime can be classified as MILD if $T_{max} - T_{in} < T_{si}$, where, T_{max} is the maximum system temperature, T_{in} is the inlet temperature in a well-stirred reactor, and T_{si} is the self-ignition temperature of the fuel mixture. The application of this approach to a semi-industrial furnace is not straightforward. However, this definition can be applied locally inside the furnace for the present work. Therefore, based on the analysis presented by Ferrarotti et al. [66] for the same furnace, this criterion is applied to different fuel mixtures. As suggested by Ref. [66], the air inlet temperature (T_{air}) is considered as inlet temperature. In the present work, the air inlet temperature is the temperature after the air passes through the heat exchanger. This cannot be measured directly and instead calculated following the heat balance of the heat exchanger, as mentioned in section 2.4. T_{si} is predicted using commercial software, ANSYS Chemkin-Pro 2019 R3, by analysing the ignition behaviour of $CH_3OCH_3/CH_4/H_2$ mixtures in a constant volume reactor without considering any heat losses [72]. For the present work, this approach is applied locally inside the furnace, where the assumption of zero heat losses can hold. The reaction mechanism NUIGMech 1.1 [73] is used for the combustion of DME mixtures. Table 6 ($\phi = 0.8$) and 7 ($\phi = 1$) present various test cases' classifications per the MILD criterion's

Table 5 – Energy balance of the furnace for test cases, D100, D25M75, and D25H75.

P [kW]	D100	D25M75	D25H75
P_{th}	15.00	15.00	15.00
P_{cool}	6.50	6.50	6.50
P_{walls}	3.51	3.50	3.67
P_{rad}	2.88	2.96	2.92
P_{exh}	2.13	2.24	2.19
ΔP	0.00	0.18	0.23

Table 6 – Classification of test cases based on the MILD criterion at $\phi = 0.8$. T_{max} refers to the maximum measured temperature.

Test case	ϕ	T_{max} (K)	T_{in} (K)	T_{si} (K)	MILD
T1	0.8	1423	942	643	✓
T2	0.8	1418	940	811	✓
T3	0.8	1388	936	853	✓
T4	0.8	1385	935	870	✓
T5	0.8	1351	930	880	✓
T6	0.8	1587	942	745	✓
T7	0.8	1695	952	824	✓

Table 7 – Classification of test cases based on the MILD criterion at $\phi = 1$. T_{max} refers to the maximum measured temperature.

Test case	ϕ	T_{max} (K)	T_{in} (K)	T_{si} (K)	MILD
T1	1	1451	994	623	✓
T2	1	1430	991	792	✓
T3	1	1416	990	821	✓
T4	1	1367	990	846	✓
T5	1	1330	986	861	✓
T6	1	1561	998	720	✓
T7	1	1630	998	802	✓

definition. As shown in Tables 6 and 7, all test cases for $\phi = 0.8$ and 1 are in the MILD regime as per the definition of [45]. It is to be noted that a case could be MILD and not be entirely flameless when there is a visible flame structure present inside the furnace. It is because the definition of MILD is related to the maximum temperature rise and mixture inlet temperature, which could still be satisfied even if a visible flame front is present. This phenomenon can occur with hydrogen present in the fuel mixture and will be discussed in the later sections.

Experimental results

This section presents the effect of fuel composition on in-furnace temperatures, OH* chemiluminescence, and pollutant emissions. Initially, a comparative analysis between the flame and flameless modes is presented for pure DME combustion. In the later sections, different fuel mixtures are investigated in flameless mode.

Characteristics of dimethyl ether in flame and flameless modes

Fig. 3 compares averaged measured temperatures in flame and flameless modes at an equivalence ratio of 0.8. The profile in flame mode (Fig. 3a) is characterised by a temperature peak close to the burner exit plane and a continuous reduction at higher axial distances. It is to be noted that due to hardware limitations, the first assessable position for temperature measurement was 70 mm from the burner exit.

In conventional combustion mode, the air/fuel mixture was ignited in the partially premixed manner in this burner at 21% O_2 level and a flame was anchored at the burner exit. This can be confirmed by averaged OH* chemiluminescence and direct flame photograph as shown in Fig. 4a and b. The high-temperature illuminating burner exit area can be seen in Fig. 4b. Indeed, in flame mode, the reaction zone was formed close to the burner exit and characterised by high-intensity counts. The maximum temperature measured was 1763 K at 70 mm from the burner exit. It increased with ϕ, due to enhanced reactivity and reached 1804 K at stoichiometric conditions, as shown in Fig. 5.

On the other hand, in flameless mode, instead of igniting close to the burner, combustion stabilised in the furnace downstream due to delayed oxidation, and hence a lift-off of the reactive region was observed. In a flameless regime, dilution of the reactive mixture due to recirculation of hot combustion products leads to reduced oxygen availability. Therefore, a delayed and slow combustion reaction occurs, leading to a distributed reaction zone. As indicated in Fig. 4a, the reaction zone stabilised at 300 mm downstream in flameless mode. It is to be noted that no visible flame was observed with a normal camera while burning pure DME in flameless mode. Instead of a shining burner exit, as shown in Fig. 4b, a cooled burner exit was observed in flameless mode (Fig. 4c). In highly diluted conditions of a flameless regime, the signals from the reaction region are very weak compared to radiations of the visible spectrum coming from

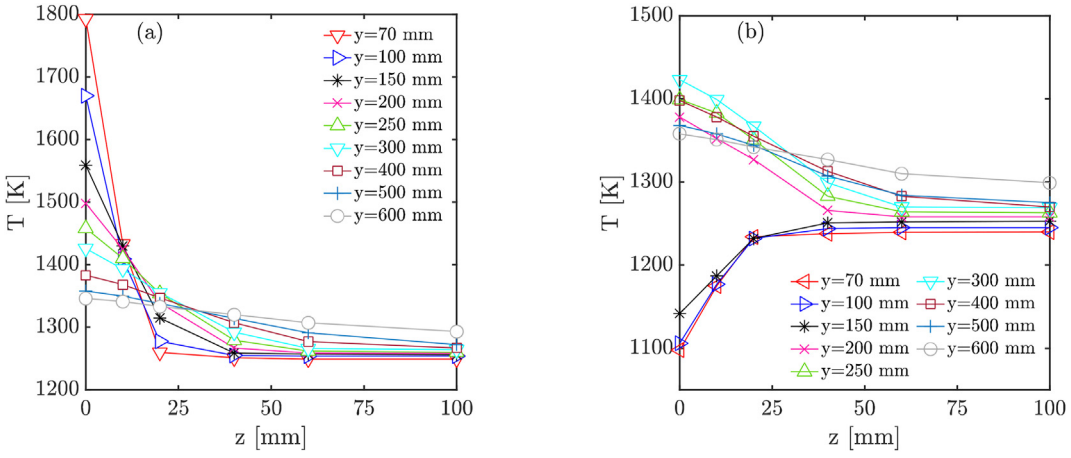

Fig. 3 – Comparison of averaged measured temperatures along the axial direction of furnace between (a) flame mode and (b) flameless mode for pure DME and $\phi = 0.8$.

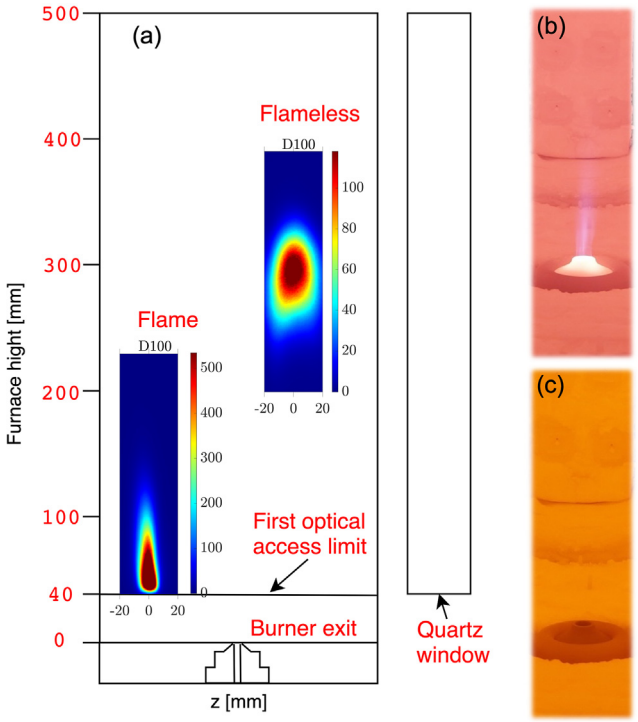

Fig. 4 – (a) Comparison of averaged OH* intensity between flame and flameless mode. Units of OH* is in counts, photographs for D100 in (b) flame mode and (c) flameless mode. $\phi = 0.8$.

hot furnace walls. However, reactions are still happening with relatively less heat release and weak chemiluminescence signals occurring in the ultraviolet range. When an OH* interferential filter is employed, it captures the ultraviolet signal while avoiding the intense visible spectral radiations from furnace walls. It is to be noted that the reaction region was relatively much less intense, wider, and more uniform compared to flame mode. The position of the reactive region was further verified by measured temperatures, as shown in Fig. 3b. It can be observed that a maximum temperature of 1423 K was recorded at 300 mm from the burner exit, which is in correspondence with the position of the reaction zone.

For the present study, exhaust gas was sampled to measure CO, NO, CO_2, H_2O, O_2, and NO_2. Fig. 6 shows the dry NO levels corrected to a 3% O_2 level for flame and flameless modes. NO decreases by two orders of magnitude for all equivalence ratios when the burner switches from the flame to the flameless regime. Indeed, NO is in single digit for all equivalence ratios (recorded as 2.2 ppm, 9.6 ppm and 7 ppm, respectively, for $\phi = 0.8$, 0.9, and 1). Suppression of temperature peaks and more uniform thermal field are the primary reason for such low NO levels in flameless mode. In flame mode, the thermal route is the dominant source of NO due to high peak temperatures ($\approx$1800 K) close to burner exit. However, in the flameless regime, NO is primarily formed via N_2O routes, as [74] discussed for a lab-scale burner.

Figs. 7 and 8 show the variation of measured temperature and OH* chemiluminescence for D100 in flameless mode with

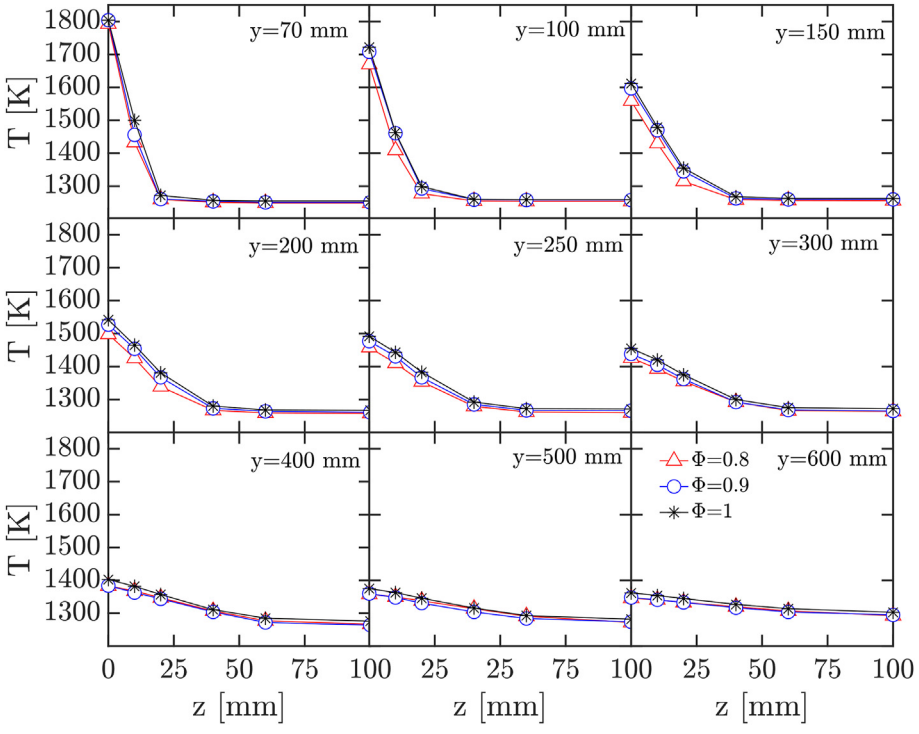

Fig. 5 – Variation of measured average temperature in flame mode for varying ϕ. y coordinate refers to the furnace height. Fuel: D100 and maximum average uncertainty in experiment = 17 K.

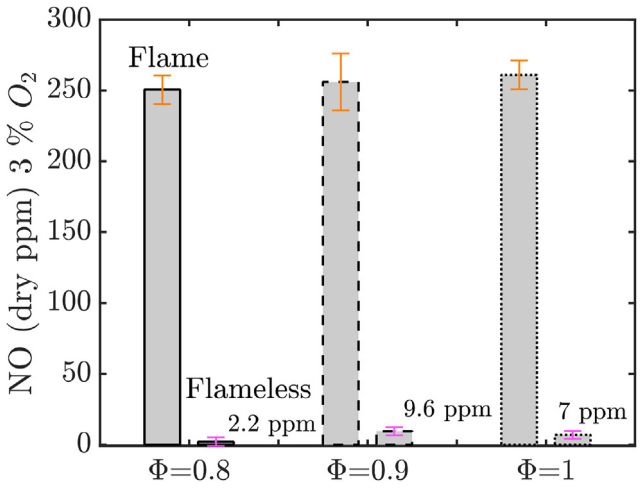

Fig. 6 – Comparison of measured dry NO emissions between flame and flameless modes.

varying equivalence ratios. For all ϕ, the temperatures appear to peak at 300 mm from the burner exit, which can be quantitatively confirmed from the OH* images shown in Fig. 8. Maximum temperatures of 1423 K, 1430 K and 1451 K were recorded for ϕ, 0.8, 0.9 and 1, respectively. Higher temperatures were recorded at stoichiometric conditions at nearly all axial locations. The reaction zone appears to be more intense as the equivalence ratio increases from 0.8 to 1, indicating the rise in system reactivity.

As shown in Fig. 8, the OH* distribution is not perfectly symmetric. This can be attributed to the tiny gap of 2 mm between fuel and air nozzles for the given injection geometry. Since the air momentum was very high, a slight disturbance created due to this narrow gap could cause considerable deviation in the reactive structure. Upon close inspection, it can be observed that for D100, the position of the reactive region is independent of the equivalence ratio except with just a few millimetres descent towards the burner exit at $\phi = 0.9$. Since this effect is minor, it does not affect the position of the maximum recorded temperature. However, the effect of the equivalence ratio on the position of the reaction zone was observed to be much more significant for dimethyl ether-methane mixtures for similar operating conditions, as will be discussed in the following sections.

Fig. 9 shows dry NO (corrected to 3% O_2) and dry CO_2 for varying ϕ. NO appears to peak at $\phi = 0.9$. Further increasing the air excess results in low overall temperature inside the furnace due to reduced reactivity. However, it also increases the availability of O radicals, thereby enhancing the NO via N_2O routes. These two combined results lead to reduced NO levels in a lean condition ($\phi = 0.8$). At stoichiometric conditions, the prompt route becomes more pertinent, and NO formation through N_2O channels becomes less significant [66]. These NO formation pathways are further explained in detail using a skeletal Chemical Reactor Model later in this paper (see section 4.2). More than 10% CO_2 was recorded for all equivalence ratios, higher than reported in the same furnace while burning the pure methane [66]. For all ϕ, no CO, NO_2, and unburned DME were measured.

It can be concluded from the above discussion that burning pure dimethyl ether in flameless mode indeed produced single-digit NO. However, CO_2 was relatively higher than methane for similar input conditions [66]. In the next section, further

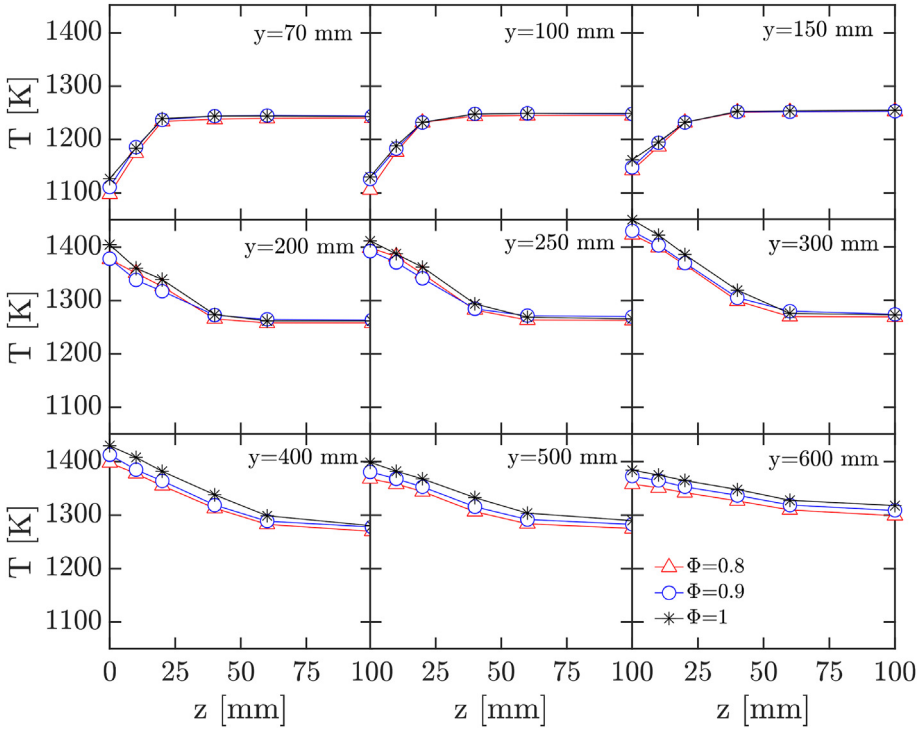

Fig. 7 – Measured average temperatures in the flameless mode for varying ϕ. Fuel: D100.

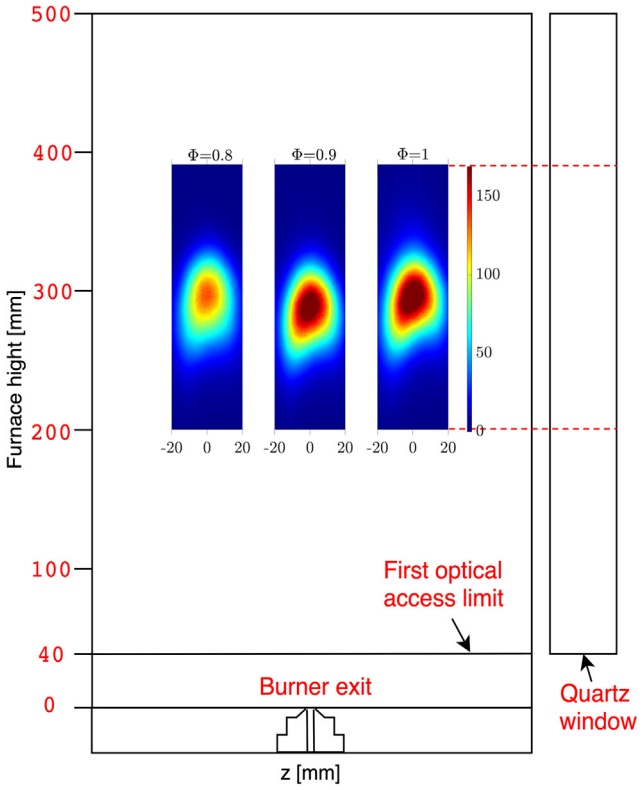

Fig. 8 – Averaged OH* chemiluminescence in flameless mode for varying equivalence ratios; fuel: D100. All images are normalised with respect to the maximum intensity count.

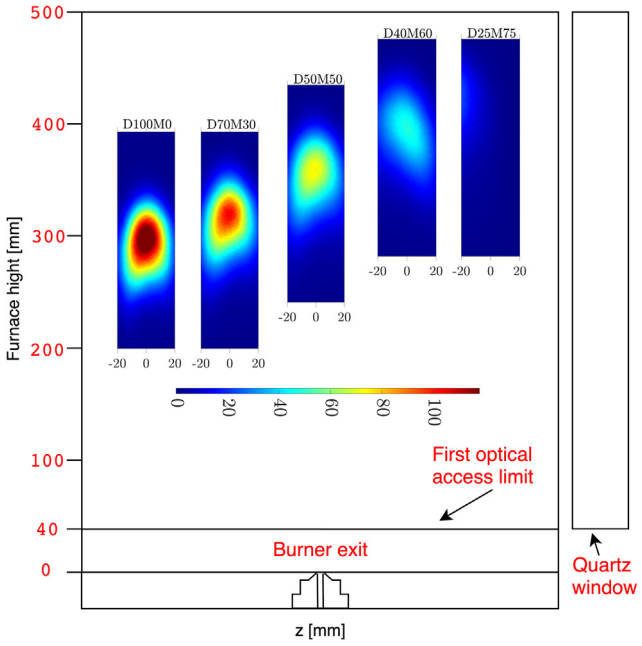

Fig. 10 – Averaged OH* contours with varying CH_4 content. $\phi = 0.8$, DxMy represents x % (vol.) of CH_3OCH_3 and y % (vol.) of CH_4.

reduction of CO_2 and complete elimination of NO through methane addition are investigated.

Characteristics of dimethyl ether-methane mixtures in flameless mode

For the present study, methane was progressively added to dimethyl ether, and its effect was assessed for different equivalence ratios through OH* chemiluminescence and temperatures. Fig. 10 displays averaged measured OH* at a fixed $\phi = 0.8$ and for different concentrations of CH_4.

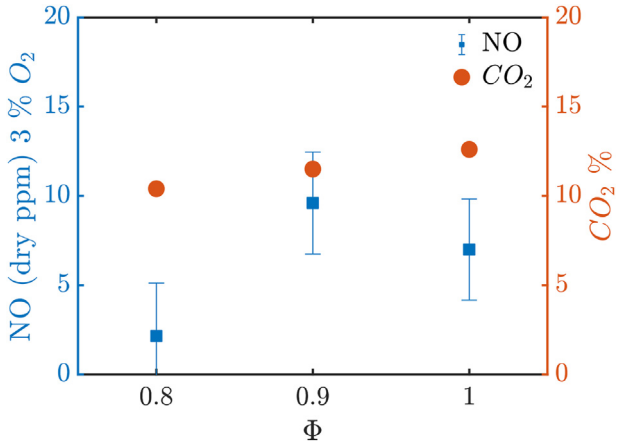

Fig. 9 – Comparison between NO and CO_2 for D100 and varying equivalence ratio.

For better comparison, the scale for all fuel mixture compositions has been kept constant (normalised to maximum intensity counts). DME is a highly reactive gas with a lower ignition delay than methane. Pure DME (D100M0) produced a minimum lift-off of 250 mm and a wide and elongated reaction region (Fig. 10). Therefore, it can be argued that the reactions are not mixing controlled, and chemistry also plays a role. This condition can be assumed to be both mixing and chemistry controlled.

As shown in Fig. 10, the reaction region moves downstream when methane is progressively added to the fuel stream. Adding methane into DME resulted in higher ignition delay times and reduced reactivity of fuel mixtures. Therefore, combustion stabilised further away from the burner, and the reaction zone became less intense. This effect was more prominent at a higher concentration of CH_4 ($\geq$ 60%), confirming the reduced reactivity of the fuel mixture. This delayed reaction facilitated enough recirculation before the ignition's commencement, which can be confirmed by analysing the temperatures close to the burner exit for all equivalence ratios. The temperatures were relatively higher for higher methane content due to increased recirculation, as shown in Figs. 11, 12 and 14. At a very high concentration of methane (D25M75), the reaction zone became almost invisible; however, it might be situated just below the roof of the furnace (y $\geq$ 500 mm), which was not accessible for the optical measurements. This condition can be considered an ideal flameless with high ignition delay times (see section 4.1). Indeed, combustion becomes chemically controlled, and mixing has a negligible role.

Temperature profiles corresponding to the operating conditions of Fig. 10 are presented in Fig. 11 for different axial

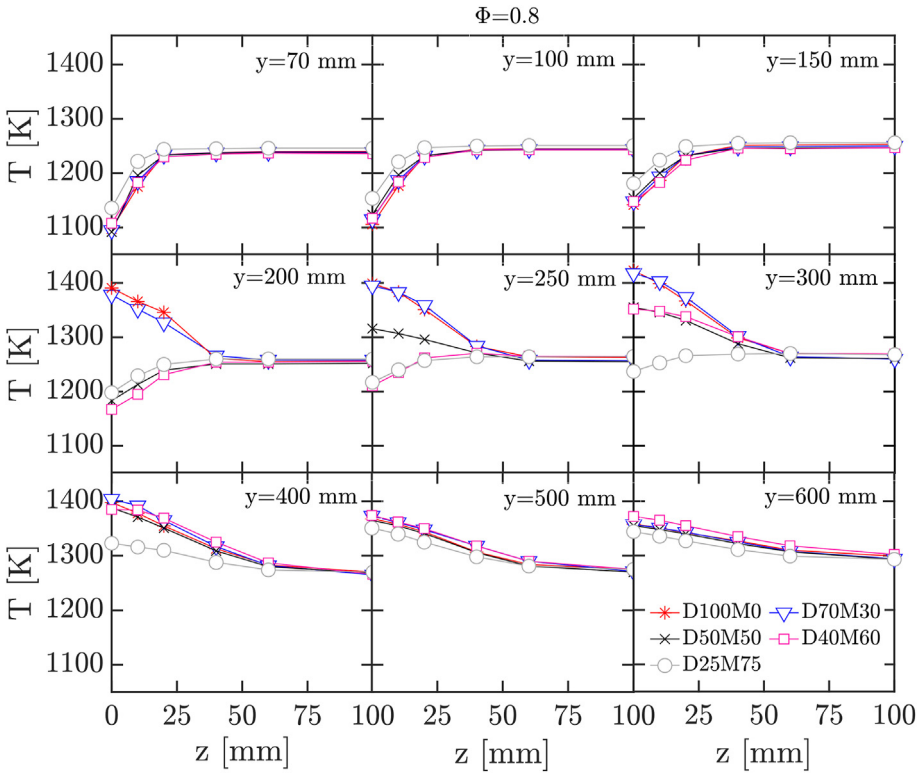

Fig. 11 – Measured average temperatures for DME/CH_4 mixtures in the flameless mode at $\phi = 0.8$. DxMy represents x % (vol.) of CH_3OCH_3 and y % (vol.) of CH_4.

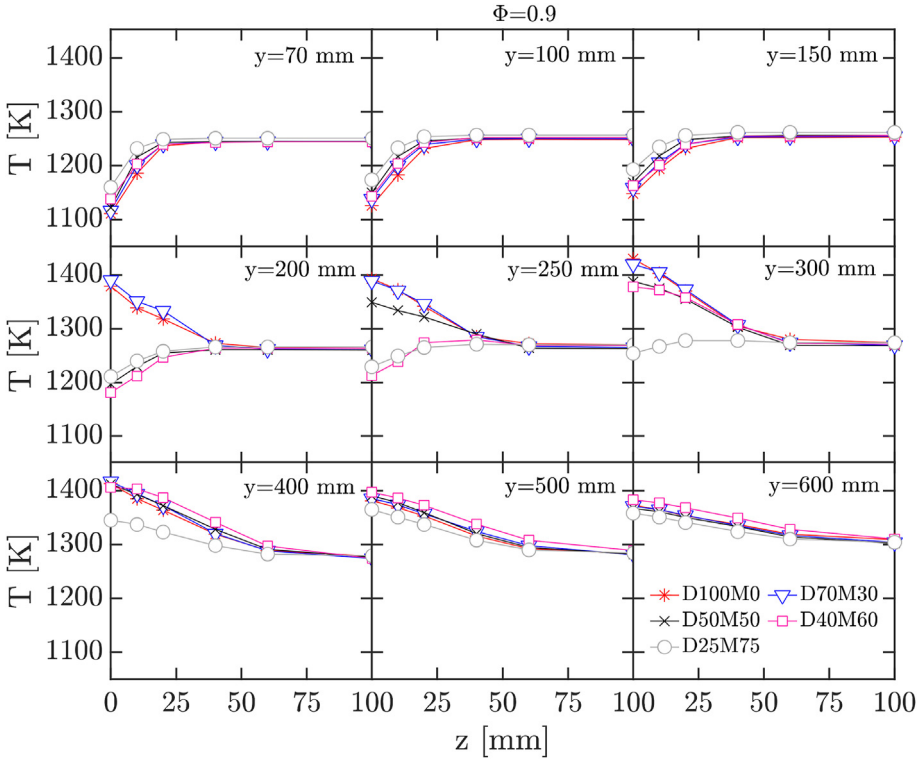

Fig. 12 – Measured average temperatures for DME/CH_4 mixtures in flameless mode at $\phi = 0.9$. DxMy represents x % (vol.) of CH_3OCH_3 and y % (vol.) of CH_4.

positions inside the furnace ($70\ mm \leq y \leq 600\ mm$). The D25M75 case shows a uniform temperature profile with a peak temperature of 1351 K at 500 mm. Therefore, the position of the reactive region is located between 500 mm and 600 mm, which was not visible from the chemiluminescence images in Fig. 10. For all the studied fuel mixture compositions at $\phi = 0.8$, D100M0 and D70M30 led to similar levels of maximum temperatures of around 1420 K at 300 mm, despite a relatively weaker reaction region for D70M30. Similar behaviour for maximum temperatures was also observed for $\phi = 0.9$, as shown in Fig. 12, which makes this effect related to the lean condition of the fuel-air mixture ($\phi = 0.8$ and 0.9). Stoichiometry does affect this behaviour, as seen in Fig. 14, where the maximum peak temperature was observed only for the pure DME case followed by lower fractions of DME.

It can also be observed from Fig. 11 that peak temperature drops significantly between D70M30 and D50M50, indicating that the effect of CH4 addition starts dominating the flame structure at this point. Temperatures for D100M0, D70M30, D50M50, D40M60, and D25M75 peak at 300 mm (1423 K), 300 mm (1418 K), 400 mm (1388 K), 400 mm (1385 K), and 500 mm (1351 K) respectively. As shown in Fig. 12, it is observed that the temperature field at $\phi = 0.9$ behaves similarly to $\phi = 0.8$ concerning maximum temperatures and their corresponding positions. Indeed, the structures of the reactive region for $\phi = 0.9$ were like that of $\phi = 0.8$; therefore, they are not presented here.

Fig. 13 presents the averaged OH* chemiluminescence for different fuel mixture compositions at the stoichiometric condition, indicating that stoichiometry significantly affects flame structure when CH_4 is added to DME. Compared to $\phi = 0.8$, the reactive region faded strongly upon methane addition. Moreover, the downward shift of the reactive region was more significant under stoichiometric conditions. The reduced air availability resulted in a delayed ignition of reactant mixture in a highly diluted environment, leading to more distributed temperatures at $\phi = 1$ compared to lean conditions. It is to be noted that even D40M60 represents the ideal flameless condition at stoichiometric condition, i.e., an almost invisible reaction zone in the optically accessible region. As seen in Fig. 14, both D40M60 and D25M75 show uniform temperature profiles with peak temperatures not exceeding 1350 K.

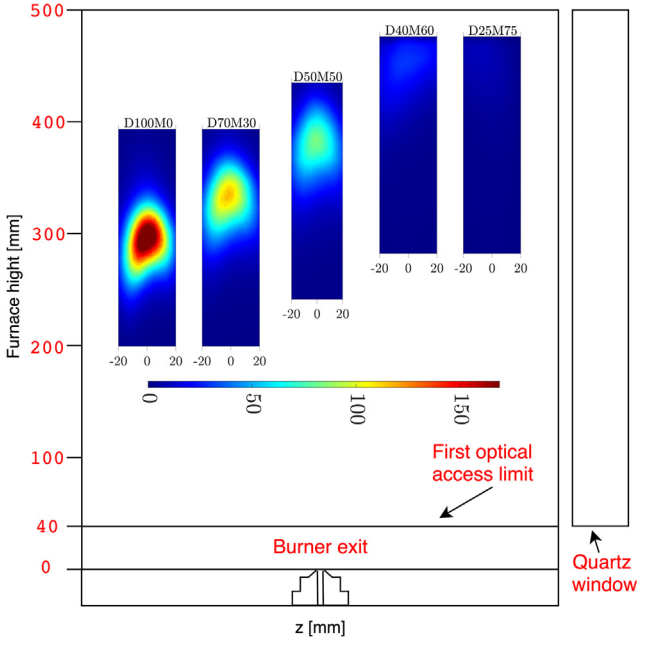

Fig. 13 – Averaged OH* contours with varying CH_4 content and $\phi = 1$, DxMy represents x % (vol.) of CH_3OCH_3 and y % (vol.) of CH_4.

Fig. 14 shows the averaged measured temperatures at $\phi = 1$ for different fuel mixture compositions. Maximum temperatures of 1451 K (300 mm), 1430 K (400 mm), 1416 K (400 mm), 1367 K (600 mm), and 1330 K (600 mm) were observed for D100M0, D70M30, D50M50, D40M60, and D25M75 respectively. For fuel mixtures of DME/CH_4, relatively smoother temperature profiles are observed at $\phi = 1$, confirming the observations from OH* chemiluminescence in Fig. 13.

From temperature distributions at different equivalence ratios, it can be observed that fuel mixtures with relatively large CH_4 content exhibit a more uniform temperature distribution. This is mainly due to increased ignition delay times which facilitates more recirculation, as discussed in the preceding paragraphs. A discussion on ignition delay times of DME/CH_4 mixtures is provided in section 4.1. Further, it will be shown in the following sections that beyond a certain limit, the addition of CH_4 may cause incomplete combustion, leading to CO emissions.

The temperature distribution and OH* chemiluminescence can be linked to draw conclusions about the structure of the reacting region. At stoichiometric conditions, up to 50% methane addition to DME, the reactive region moved downstream from 300 mm to 400 mm, corresponding to the maximum temperature position. Lowering methane content to 30% (D70M30), the reactive region was positioned between 300 mm and 400 mm, and the maximum temperature point was at 400 mm. Similarly, the temperature for D100M0 and D70M30 peaked at 300 mm for $\phi = 0.8$, corresponding to the position of the reactive region (Fig. 10).

Fig. 15 shows the measured averaged values of NO and CO_2 emissions for variable CH_4 content in the fuel mixture. NO is in dry ppm, normalised to 3% O_2, while CO_2 is in vol%. For all investigated fuel mixtures, NO stayed below 10 ppm. Such conditions are typically presented as flameless conditions in lab-scale studies wherein no visible flame was observed if NO is below a threshold value (~10 ppm) [75]. Indeed, this can be applied here because of low NO (less than 10 ppm) and non-visible flame. Also, the reactive region was located at 300 mm and above for all cases, while temperature gradients were smooth with low maximum temperatures. The temperature field analysis allows us to conclude NO formation that the thermal pathway was not the primary NO producer, thus leaving N_2O routes as the possible major source of NO. It was observed that methane addition resulted in lower NO compared to pure DME, mainly due to lower temperatures achieved. However, the formation pathways of NO did not change substantially as discussed in detail in section 4.2.

As discussed in previous sections, CH_4 addition was aimed at possible reduction of NO and CO_2, and indeed, it was found to help lower both but by different margins. NO was reduced by almost 100% as soon as CH_4 is blended with DME, even by a

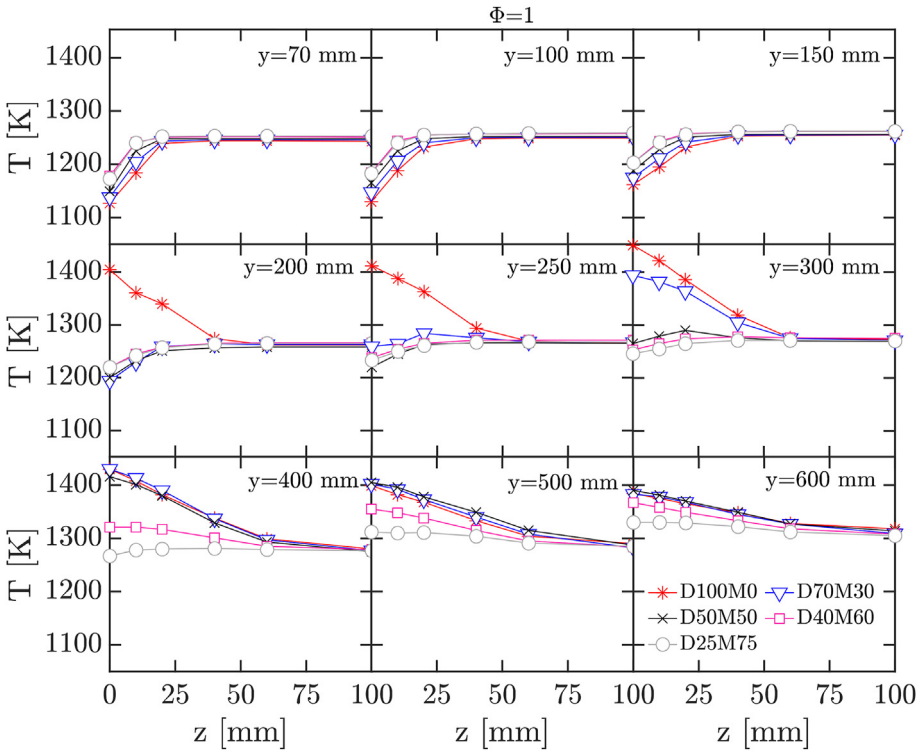

Fig. 14 – Measured average temperatures for DME/CH_4 mixtures in flameless mode at $\phi = 1$. DxMy represents x % (vol.) of CH_3OCH_3 and y % (vol.) of CH_4.

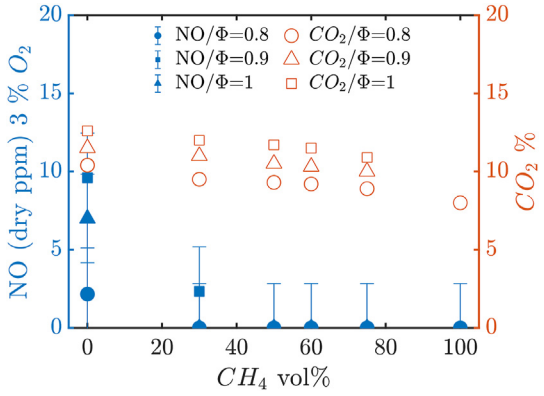

Fig. 15 – Variation of NO and CO_2 for varying content of CH_4 in the fuel mixture.

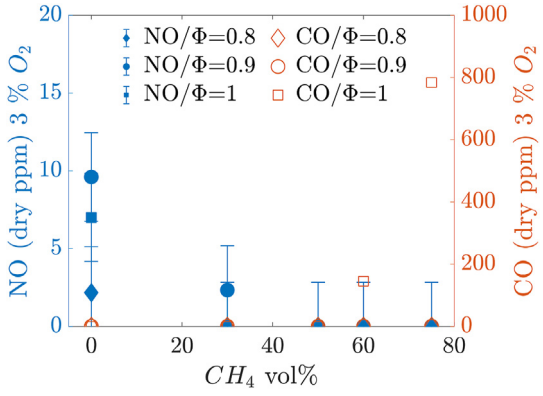

Fig. 16 – Variation of dry NO and CO for varying content of CH_4 in fuel mixture.

small content. For D70M30, a small amount of NO (~2 ppm) was measured only at $\phi = 0.9$. For the rest of the conditions with CH_4 blending, NO was not found in exhaust gases. CO_2 was lowered by 11% for D50M50 (9.3% CO_2), 14% for D25M75 (8.9% CO_2), and 23% for D0M100 (8% CO_2).

Fig. 16 shows the combined variation of NO and CO for varying CH_4 content. Both are in dry ppm and corrected to 3% O_2. CO was not observed in the exhaust gases for most of the investigated cases. However, at stoichiometric conditions of D40M60 and D25M75, a large amount of CO was measured in the exhaust, as indicated in Fig. 16. The reduced availability of oxygen led to lower combustion efficiency in these cases, indicated by the presence of CO in the exhaust gases.

Characteristics of dimethyl ether-hydrogen mixtures in flameless mode

Hydrogen was added to DME to lower the CO_2 while not increasing the NO levels significantly. Indeed, H_2 addition can lead to higher NO emissions [66]; however, as the burner operates in flameless mode, that possibility can be avoided. This dilution is also essential because of the renewable nature of both H_2 and DME, and this fuel mixture can be a potential renewable synthetic fuel. Fig. 17 shows the averaged OH* chemiluminescence for DME/H_2 mixtures for $\phi = 0.8$ and 1. Two different mixtures compositions were chosen for the present study, D50H50 (50-50 DME/H_2 by vol%) and D25H75 (25–75 DME/H_2 by vol%). For D50H50, H_2 provides only 15.40%

of the total input power. The case of D25H75 allows to investigate the characteristics of the system when H_2 starts affecting the flame structure considerably (roughly 35% of the total power is provided by H_2).

Fig. 17 shows that the reactive region moves progressively towards the fuel nozzle due to H_2 addition. In addition, H_2 addition made the OH* region more intense and localised. This is consistent with the higher reactivity and diffusivity of hydrogen. Further discussion on the role of reactivity and diffusion on H_2-doped flame structures is presented in section 4.1. The high-intensity region of the OH* chemiluminescence signal increased with an increase in the ratio of hydrogen. This description is in line with the measured temperatures as shown in Figs. 19 and 20 which clearly show that temperature increased upon hydrogen addition. Moreover, it can also be observed from Fig. 17 that for higher hydrogen content (i.e., 75% vol. H_2), the reactive region becomes elongated. It is due to the higher impulse of the fuel jet, which is necessary to keep the thermal power constant at 15 kW. This results in increased penetration of fuel jets and therefore an elongated reactive region. It is to be noted that the reactive region moved closer to the nozzle exit as H_2 was added to DME, and therefore the system eventually loses its flameless characteristics since combustion commences before enough recirculation and dilution have taken place.

In hydrogen diluted flames (D25H75), opposite to the methane-diluted flames, the reactive region was more intense and narrower. It moved closer to the burner exit as the equivalence ratio was increased from 0.8 to 1. However, the flame was never found to be attached to the burner for the investigated fuel mixture types. At D50H50, the flame was not hydrogen dominated, and the reactive region did not move towards the burner when the equivalence ratio increased from 0.8 to 1. It can be argued that for flames with higher hydrogen concentration, the lift-off of the reactive region is less than 100 mm. Such flames can be assumed to be controlled more by mixing compared to chemistry, and, in such cases, the Damköhler number may become greater than one. As discussed in section 3.1, the asymmetricity in OH* distribution can be attributed to the narrow gap available (2 mm) for airflow between fuel and air nozzles. Photographs for different fuel mixtures at $\phi = 1$ are shown in Fig. 18. D100H0 is characterised by non-visible flame (Fig. 18a). Visible flame appeared (position marked by black circles) as soon as hydrogen started getting added to the fuel stream. This small diffusion flame is expected to increase peak temperatures which are presented in the following sections.

Fig. 19 presents the averaged measured temperature at equivalence ratio, $\phi = 0.8$ for varying content of H_2 in DME. The temperature peaked at 100 mm and 200 mm for D25H75 and D50H50, respectively, with maximum values recorded as 1695 K and 1587 K. It can be observed here that the presence of flame front due to H_2 addition is associated with high-temperature peaks. Higher reaction rates associated with H_2 may result in a mixing-controlled combustion regime. It is to be noted that, unlike in CH_4 diluted cases, the temperature at

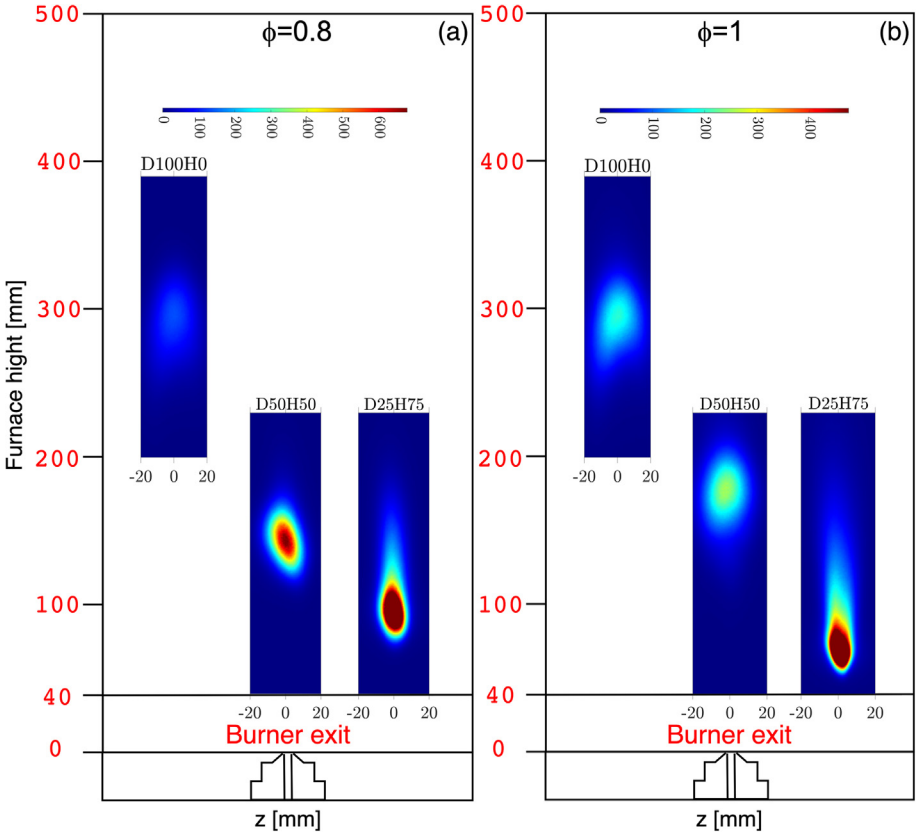

Fig. 17 – Averaged OH* contours with varying H_2 content at (a) $\phi = 0.8$ and (b) $\phi = 1$, DxHy represents x % (vol.) of CH_3OCH_3 and y % (vol.) of H_2.

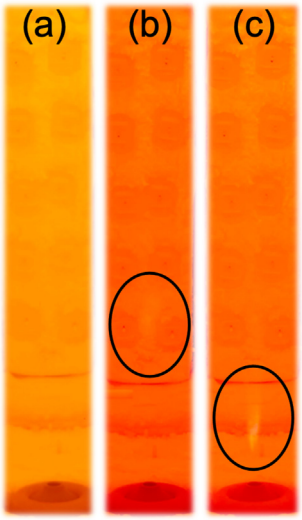

Fig. 18 – Photographs for (a) D100H0, (b) D50H50, and (c) D25H75.

higher axial distances (y ≥ 200 mm) was less sensitive to variable H_2 content. Similar behaviour was also noticed at the equivalence ratio, $\phi = 1$, as shown in Fig. 20.

It can be observed upon a comparison of Figs. 19 and 20 that with H_2 addition and for y ≤ 200 mm, temperatures are lowered with increasing equivalence ratio (except for D25H75 and y = 70 mm), which is opposite to what was observed with CH_4 addition. For D25H75, the reactive region was close to the first measurement point, i.e., 70 mm, and a higher temperature was measured for $\phi = 1$ compared to $\phi = 0.8$. This temperature distribution for y ≤ 200 mm is supported by the OH* distribution. Fig. 17 indicates that a decrease in average intensity count is observed when ϕ is increased from 0.8 to 1. Maximum temperatures for D25H75 and D50H50 at $\phi = 1$ were measured at 100 mm (1630 K) and 200 mm (1561 K). Moreover, for axial distances greater than 200 mm, measured temperatures at $\phi = 1$ were greater than those at $\phi = 0.8$, confirming the localised effect of H_2 in the near nozzle region.

Fig. 21 shows the measured NO and CO_2 emissions for varying content of H_2 in the fuel mixture at different equivalence ratios. The reduction of CO_2 is predominant at higher H_2 concentrations. At $\phi = 0.8$, CO_2 was lowered by about 18% at 50% H_2 (D50H50), about 37% at 75% H2 (D25H75), and 100% for pure H_2. However, it is to be noted that this reduction was achieved at the cost of increased NO emissions. At the same equivalence ratio, $\phi = 0.8$, progressively increasing NO was measured as 2.16 ppm, 10 ppm, 48 ppm, and 61 ppm, respectively, for D100H0, D50H50, D25H75, and D0H100. The results hint at the optimum level of H_2 dilution, which is approximately 50% by vol., to keep NO at around 10 ppm while lowering CO_2 by about 18%. The thermal pathway of NO became gradually more important as hydrogen concentration increases (see section 4.2). The maximum NO value due to H_2 addition was measured as 49 ppm for D25H75. It is also to be noted that no unburned DME was found in the exhaust for all the investigated cases.

Kinetic analysis

This section presents the analysis of ignition behaviour and NO formation for different fuel mixtures of pure DME, DME/

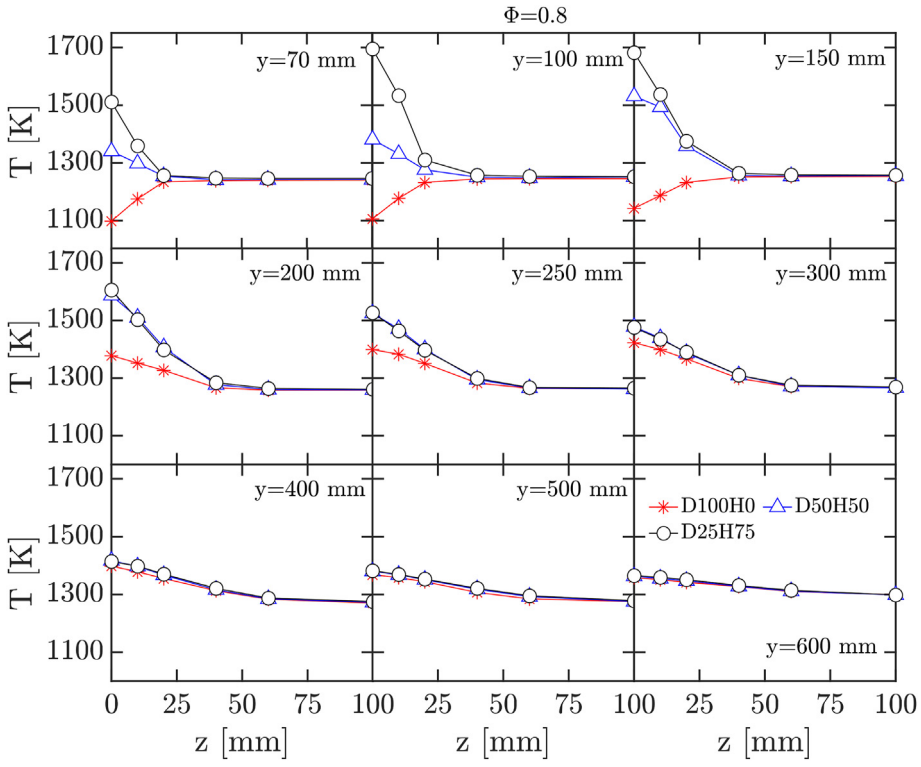

Fig. 19 – Measured average temperatures for DME/H_2 mixtures in flameless mode at $\phi = 0.8$. DxHy represents x % (vol.) of CH_3OCH_3 and y % (vol.) of H_2.

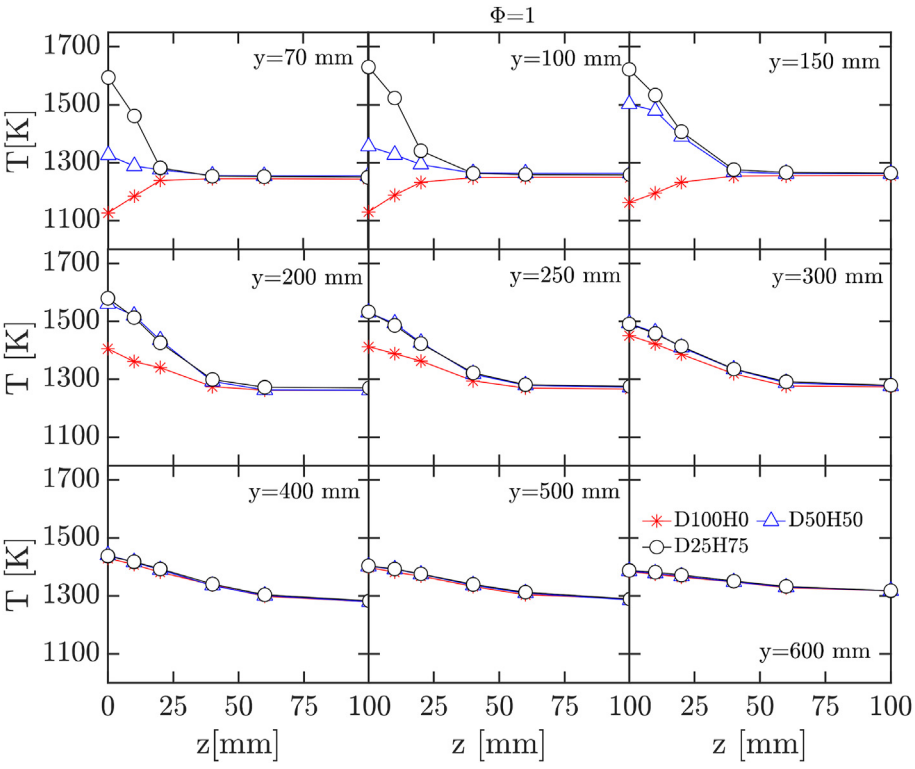

Fig. 20 – Measured average temperatures for DME/H_2 mixtures in flameless mode at $\phi = 1$. DxHy represents x % (vol.) of CH_3OCH_3 and y % (vol.) of H_2.

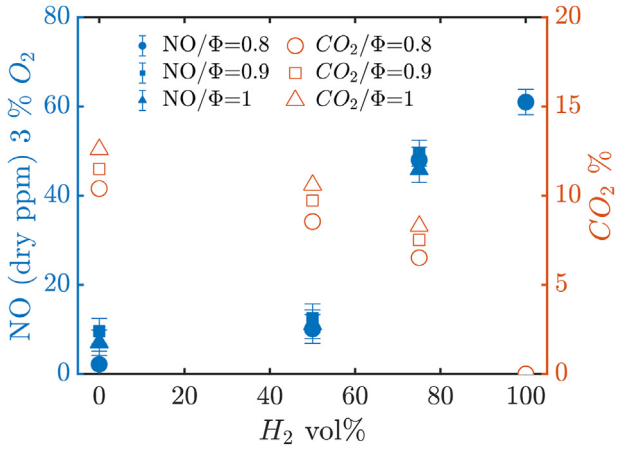

Fig. 21 – Variation of NO and CO_2 for varying content of H_2 in the fuel mixture.

CH_4, and DME/H_2. Initially, the ignition delay times are calculated using a simple batch reactor with recirculation, and later, different NO formation pathways are presented using a simplified Chemical Reactor Network.

Ignition behaviour of DME/CH_4 and DME/H_2 mixtures

Ignition analysis was performed for different DME/CH_4 and DME/H_2 mixtures at varying equivalence ratios and a fixed thermal input of 15 kW. A commercial software Chemkin Pro19 was used to analyse the kinetics of a normal batch reactor with an arbitrary recirculation (recirculation ratio, Kv = 3) to show a qualitative trend of ignition behaviour for different mixtures. The reaction mechanism NUIGMech 1.1 [73] was used for the combustion of DME/CH_4/H_2 mixtures. To analyse the effect of CH_4 and H_2 addition on DME ignition qualitatively, the ignition delay times for different fuel mixtures at varying equivalence ratios are shown in Fig. 22.

It can be observed from Fig. 22 that at $\phi = 0.8$, with methane addition, the ignition delay time shows a gradual increase when the CH_4 blending ratio is lower than 80%, followed by a steep increase. At $\phi = 1$, the steep rise in ignition delay is observed starting at 60% CH_4 addition. It means that CH_4 dilution inhibits the ignition of DME/CH_4 mixtures, and the dilution becomes more effective at $\phi = 1$, as shown in Fig. 22. On the other hand, with H_2 addition, the ignition delay time does not vary much when H_2 content is below 80% and then shows a marginal decrease. This behaviour is almost similar for all equivalence ratios, unlike the CH_4 addition. Therefore, it can be argued here that for systems with recirculation, H_2 is not effective as an ignition promotor for the range of inlet temperatures and H_2 blending ratios ($H_2 \leq 75\%$) considered in the present study.

In this study, it is mentioned in section 3.2 that with CH_4 addition, the reactive region moves downstream and becomes less intense. This is consistent with the analysis shown in the above paragraphs that the addition of CH_4 results in increased ignition delay time. A higher ignition delay ensures more recirculation within the reaction region before ignition starts, thereby creating favourable conditions for flameless combustion. As shown in Fig. 10, the effect of CH_4 addition on the

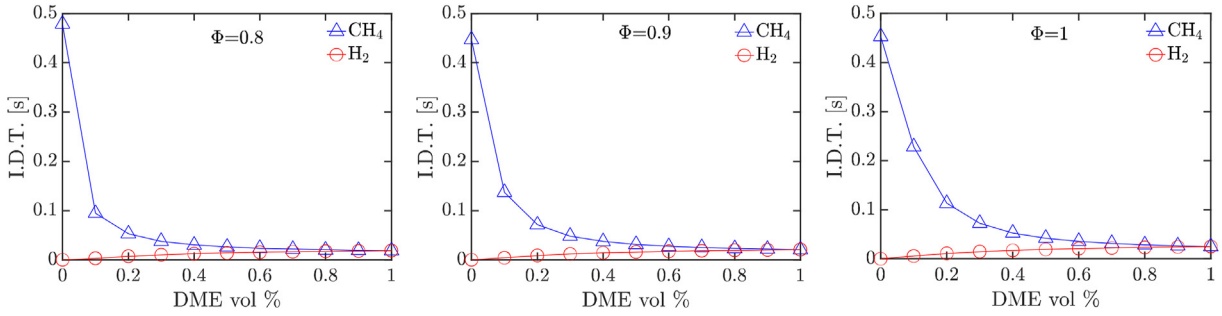

Fig. 22 – Variation of ignition delay times of DME/CH_4 and DME/H_2 mixtures for different equivalence ratios.

reactive region becomes more prominent for the D25M75 case at $\phi = 0.8$. This means a sufficient ignition delay ensures sufficient recirculation such that the combustion becomes chemically controlled and the reactive region becomes almost invisible. However, for stoichiometric DME/CH_4 mixtures, even D40M60 exhibits a chemically controlled combustion and invisible reactive region (see Fig. 13), which again proves that CH_4 addition to DME in flameless systems is more effective under stoichiometric conditions. This effect of stoichiometry is also consistent with the ignition delay time variation shown above in Fig. 22.

The effect of H_2 addition on the reactive region was opposite to that of the CH_4 addition. As shown in Fig. 17, H_2 addition makes the OH* region more intense and localised. The high-intensity region of the OH* chemiluminescence signal increases with an increase in the ratio of hydrogen. Moreover, the reactive region moves closer to the burner exit with H_2 addition. It is explained above for DME/H_2 mixtures that H_2 addition does not lower the ignition delay much for the range of H_2 blending ratios ($H_2 \leq 75\%$) considered for the present study. Hence, it can be argued that the reactivity of H_2 is not a dominant factor in the reactive region characterisation of DME/H_2 mixtures inside the present flameless furnace.

Molecular diffusion at such elevated hydrogen dilutions can also play a potential role in modifying the reactive structure of the flame. As an example, for industrial burners similar to what has been used in the present study along with similar turbulence levels, it was reported that molecular diffusion had a slight influence on the distribution of temperature and major species when H_2 was present in the system in a significant amount, as shown by Parente et al. [76]. However, its effect mostly affected the flame in a highly localised area close to the burner, where higher temperature peaks were observed, while the overall flame configuration and macrostructure were not influenced in a significant way, mainly because of the elevated turbulence level. Thus, in the test case examined in this work, the enhanced molecular diffusivity can also have a role in influencing the local temperature and species distribution close to the ignition point. However, seen the elevated velocities and the profound differences in mixtures reactivities, a combined effect of mixing and reaction rate probably remains the dominant cause of different reactive structures encountered in the experiments.

In cases where the hydrogen content is significant, there is not enough recirculation of combustion products before the ignition starts, and hence the flameless behaviour is compromised. Therefore, a flame front appears as H_2 is getting added to the fuel mixture as shown in Fig. 18, characterised by high furnace temperatures and increased NO levels. It is also to be noted that because of reduced recirculation, the combustion is not distributed and hence the width of the reactive region decreases as shown in Fig. 17. In such cases, combustion can be assumed to be controlled more by mixing than chemistry.

It can be concluded here that CH_4 addition to DME leads to a more distributed and downwardly shifted reactive region mainly due to increased ignition delay times. On the other hand, with H_2 addition, a combined effect of mixing and the reaction rate dominates, leading to a more intense, localised and upwardly shifted reaction region.

Kinetic modelling

To further investigate the effect of the different mixtures and operating conditions on NO formation from a chemical point of view, a highly simplified Chemical Reactor Network was built and simulated with the commercial software CHEMKIN Pro. The network, schematically represented in Fig. 23, consists of two Perfectly Stirred Reactors (PSRs) in series with internal recirculation. The first reactor represents the main flame, and it is modelled by an adiabatic PSR with a fixed arbitrary residence time of 1s, while the second PSR represents the post-flame area of the combustor, where heat losses are imposed. The heat losses are modelled as a boundary condition by fixing a net loss value in the second reactor, which is equal to the heat losses detected experimentally so that the temperature in the post-flame reactor is equal to the outlet temperature detected experimental value.

As the addition of both hydrogen and methane strongly influence the ignition point and consequently the amount of recirculation in the reaction zone, the recirculated mass flowrate was adjusted for all the cases by tuning its value in such a way that the temperature reached by the adiabatic PSR 1 is equal to the maximum temperature observed experimentally. The amount of flue gas entrainment, $\dot{m}_{rec}$, can be quantified in terms of the recirculation ratio K_V, as:

$$K_V = \frac{\dot{m}_{rec}}{\dot{m}_{air} + \dot{m}_{fuel}}$$

Kinetic calculations were carried out by employing two different kinetic mechanisms, namely the NUIGMech 1.1 [73] and the CRECK [77] kinetic schemes. First, the effect of the

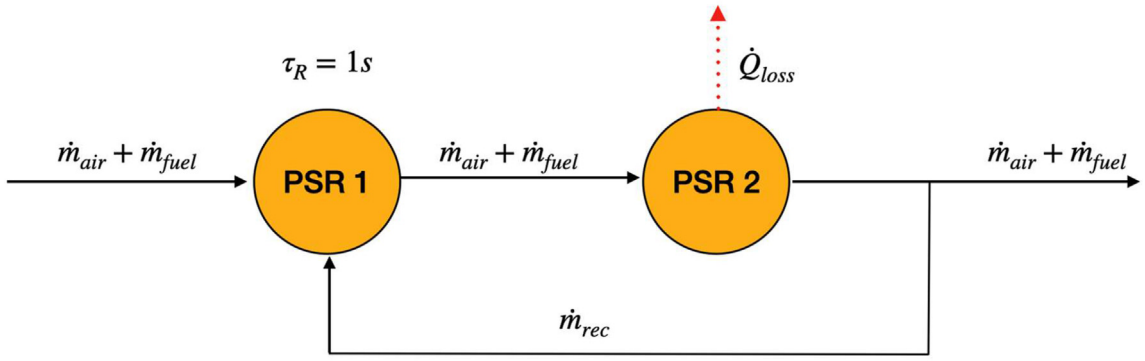

Fig. 23 – Schematic representation of the adopted Reactor Network consisting of a flame PSR with fixed residence time (PSR1) and the post flame reactor (PSR2) with a fixed volume equal to the remaining volume of the chamber.

equivalence ratio on NO formation for pure DME was investigated. Second, the effect of both hydrogen and methane addition to DME was analysed.

Effect of equivalence ratio

As observed in the experimental trends, namely from Figs. 7 and 8, the equivalence ratio did not profoundly modify the reactive structures in the furnace, producing very similar temperature profiles and, therefore, similar NO emissions (Fig. 9). The reactor network was simulated for the three different equivalence ratios ($\Phi = 0.8$, $\Phi = 0.9$ and $\Phi = 1.0$) and the recirculation ratio necessary to achieve the experimental maximum temperature was found to be $K_V = 6.75$ for all the pure DME cases. The heat losses were found to be 12.5 kW. Although the model presents a rather simple configuration, it was able to predict NO emissions with a good match on experimental data, as reported in Table 8.

The two different kinetics schemes offered slightly different results. In general, the CRECK mechanism yielded slightly lower NO values with respect to the NUIGMech 1.1, showing better predictions in the lean cases, while the NUIGMech 1.1 performed better towards stoichiometric. It is to be noted that for identical input conditions, the kinetic model predicts different values of NO for different kinetic mechanisms. In such cases, the experimental data could be crucial for better accuracy.

To deeper investigate the main kinetic phenomena governing the formation of NO, a flux analysis and a sensitivity analysis on NO formation were carried out on the flame PSR (PSR1). The two kinetic schemes did not show any structural difference; therefore, only the NUIGMech 1.1 results are reported below. Moreover, no profound changes were observed between the $\phi = 0.8$ and the $\phi = 0.9$ cases, so only the results on the $\Phi = 0.8$ and the $\Phi = 1.0$ are shown. As we can observe from both Figs. 24 and 25, most of NO emissions are formed via the N_2O route (green arrows), as a rather low temperature is encountered in the reaction region (~1450 K).

Some reburning (red arrows) is also present at both $\Phi = 0.8$ and $\Phi = 1.0$, but the predominant path appears to be the NO–NO_2 equilibrium (blue arrows) as some NO radicals are already present in the recirculated flue gases. As we can also notice from Fig. 25, some thermal NO (black arrows) is starting to form, as the temperature reached in stoichiometric conditions is slightly higher with respect to the lean case. The NO formation paths were identified following the classification provided by Glarborg et al. [78].

A sensitivity analysis on NO reactions was also performed by evaluating the normalised sensitivity coefficients for the reactions. The sensitivity coefficient $C_{S,ik}$ is defined as the sensitivity of the k-th species to the pre-exponential factor of the i-th reaction, A_i, normalised by the mass fraction of the analysed species, Y_k:

$$C_{S,ik} = \frac{(A_i \partial Y_k)}{(Y_k \partial A_i)}$$

The magnitude of the sensitivity coefficient represents the importance of the i-th reaction to the formation of the k-th species, while its sign indicates a positive (+) or negative (–) contribution. The sensitivity analysis was performed for the lean and the stoichiometric cases, and the results are displayed in Fig. 26. For both cases, NO formation appears quite sensitive to reactions involving the intermediate N_2O, namely R1, R6 and R9. As slightly rich conditions are approached, reactions involving the prompt formation route (namely R14) start to become more sensitive, as well as reactions involving CH and H radicals, since those active species become more available in the radical pool. It is also important to mention that fuel oxidation reactions, which consume OH radicals (R5, R7 and R8), have a negative sensitivity coefficient, thus inhibiting the formation of NO, since OH radicals that are consumed through fuel oxidation do not contribute to nitrogen oxidation.

Effect of fuel composition

As observed from the experiments, NO emissions were mostly enhanced by the addition of hydrogen to DME, as temperature

Table 8 – NO predicted by the reactor network model with NUIGMech 1.1 and CRECK chemical mechanisms at different equivalence ratios for pure DME.

NO dry ppm @3% O_2			
Case	Exp	NUIGMech 1.1	CRECK
$\Phi = 0.8$	2.2	4.2	1.7
$\Phi = 0.9$	9.6	6.1	3.4
$\Phi = 1.0$	7	9.43	7.1

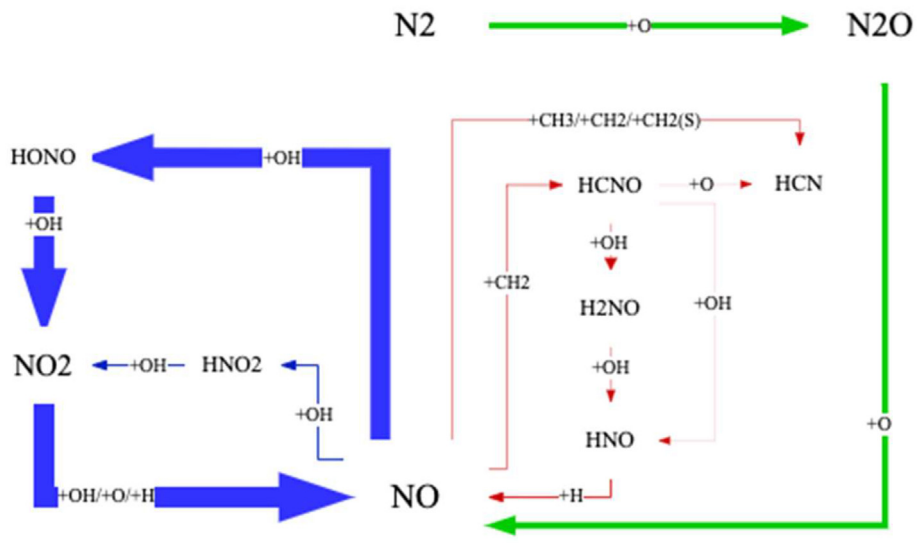

Fig. 24 – NO flux analysis for pure DME at phi = 0.8.

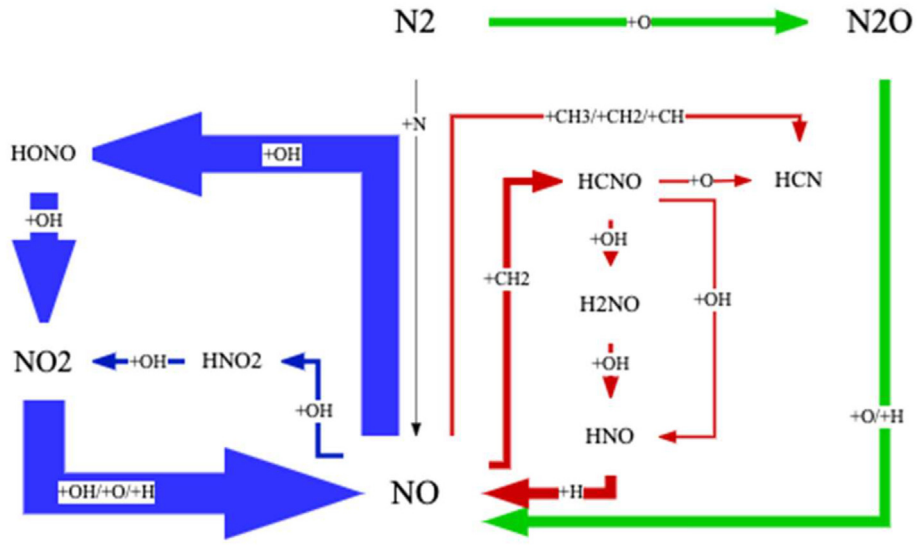

Fig. 25 – Flux analysis of NO formation for pure DME at phi = 1.0.

gradients and peaks were more pronounced. For methane addition, instead, a negative trend was observed. The chemical reactor network was used to simulate all the experimental cases investigated, namely DME-H_2 and DME-CH_4 mixtures at $\Phi = 0.8$, 0.9 and 1.0. In this case, the value of K_V necessary to replicate experimental temperatures was strongly influenced by the fuel composition (Fig. 28).

As we can observe from Fig. 27, the reactor network was able to correctly predict NO emissions within the range of experimental uncertainty for most of the fuel mixtures. At higher hydrogen content, however, the mismatch between the model and the experiments slightly increased but remained under an acceptable level. This can be related to the fact that when hydrogen is added to the fuel mixture, the combustion regime in the furnace gradually departs from the flameless regime, meaning that the approximation of the system as PSRs with internal recirculation can be compromised. However, the simple structure was also kept at higher hydrogen concentrations as it was sufficiently accurate for the scope of this work.

A flux analysis for NO formation for the 25–75% DME-H_2 case at $\Phi = 0.8$ is reported in Fig. 29. As we can observe, the thermal formation route (black arrows) is more pronounced with respect to pure DME (Fig. 24), while the reburning mechanism appears weaker, seen the scarcer availability of CH radicals. Profound differences were not encountered by comparing the 50-50 DME-H_2 with the 25–75 DME-H_2 cases; therefore, only the case with higher addition of hydrogen is analysed. A sensitivity analysis was also performed, and it is reported in Fig. 30. As we can observe, since the thermal formation pathway becomes more significant, the oxidation process leading to NO is mainly influenced by reactions involving direct oxidation of nitrogen (R20), therefore containing N radicals. NO formation appears also less influenced by reactions involving N_2O intermediate (namely R1) with

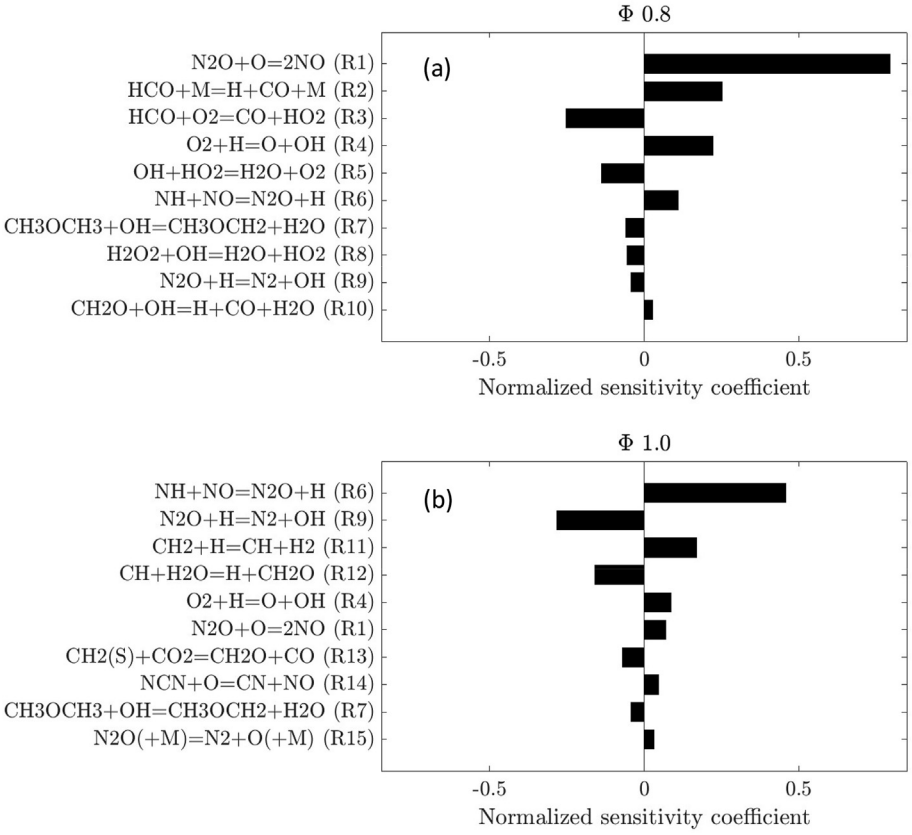

Fig. 26 – Normalised sensitivity coefficients on NO formation for two different equivalence ratios, (a) Φ = 0.8 and (b) Φ = 1.0 for pure DME.

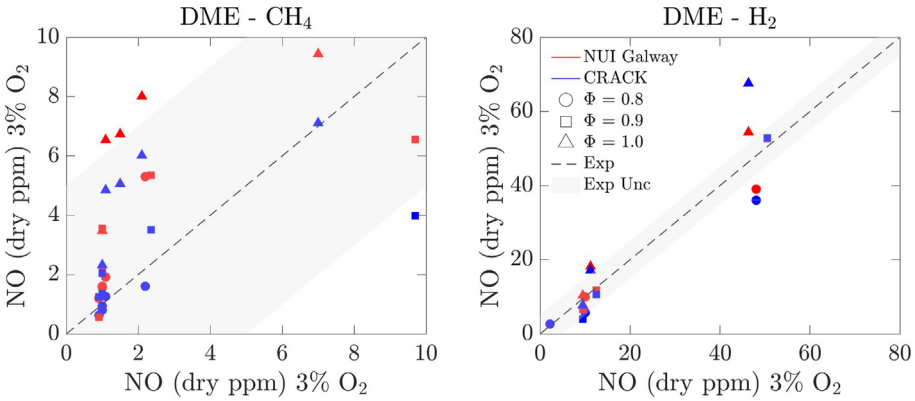

Fig. 27 – Chemical reactor network prediction of NO emissions for methane (left) and hydrogen (right) mixtures at different equivalence ratios with two different kinetic mechanisms.

respect to pure DME in lean conditions (Fig. 26a), as the temperatures reached in the reaction zone are higher for hydrogen-doped mixtures.

Regarding the addition of methane, a decrease in NO emissions was observed in the experiments, mainly because of the lower temperatures encountered. A flux analysis and a sensitivity analysis on NO emissions were performed for the 25–75 DME-CH_4 case in lean conditions and are reported in Figs. 31 and 32, respectively. The obtained results, for both the flux path analysis and the sensitivity, are very similar to the pure DME case at Φ = 0.8 (see Figs. 24 and 26a). Also, in this case, where the furnace is operating at MILD regime with a high recirculation ratio (Kv = 13), the N_2O route appears to be the dominant path for NO formation. This can also be observed from the sensitivity results, as the process is most sensitive to reactions involving N_2O (R1).

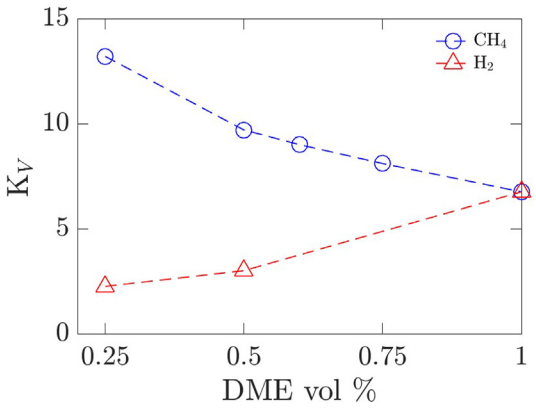

Fig. 28 – Values of K_V obtained for different DME-H_2 and DME-CH_4 mixtures.

The adopted model, even with a highly simplistic form, was useful to explain the trends obtained in the experiments and to highlight differences between the governing chemical phenomena at several DME dilution levels with different fuels. The NO–NO_2 chemical equilibrium was found to be dominant in all the cases studied, mainly due to the consistent internal recirculation in the furnace. The addition of more reactive components to DME, namely hydrogen, strongly influenced the recirculation ratio at which combustion takes place, thus shifting the furnace operation from the MILD to the conventional regime. For this reason, higher NO emissions were observed, both numerically and experimentally, since the thermal pathway becomes gradually more important as hydrogen concentration increases. On the other hand, the addition of methane highlighted an increase in the recirculation ratio within the reaction region, and the operability of the furnace in the MILD regime was not compromised.

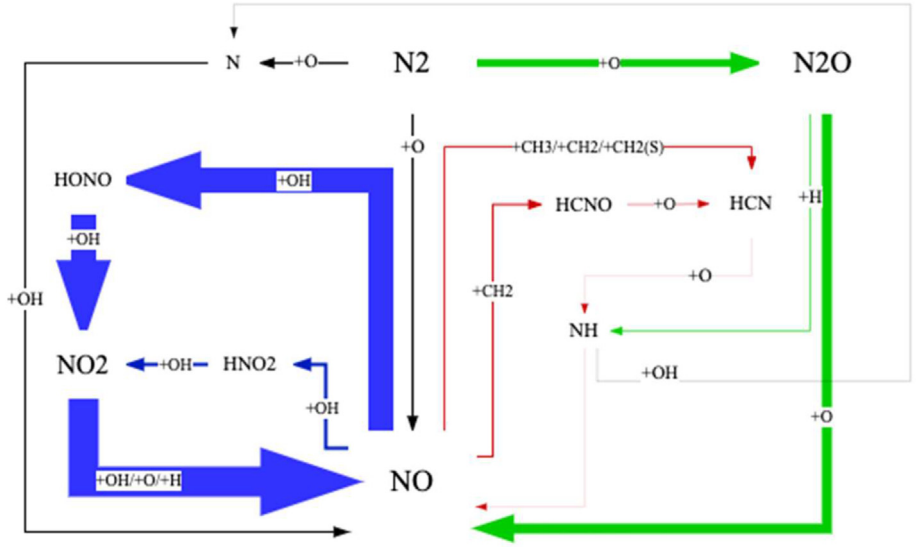

Fig. 29 – Flux analysis of NO formation for the 25–75% DME-H_2 mixture at $\Phi = 0.8$ performed with the NUIGMech 1.1 mechanism.

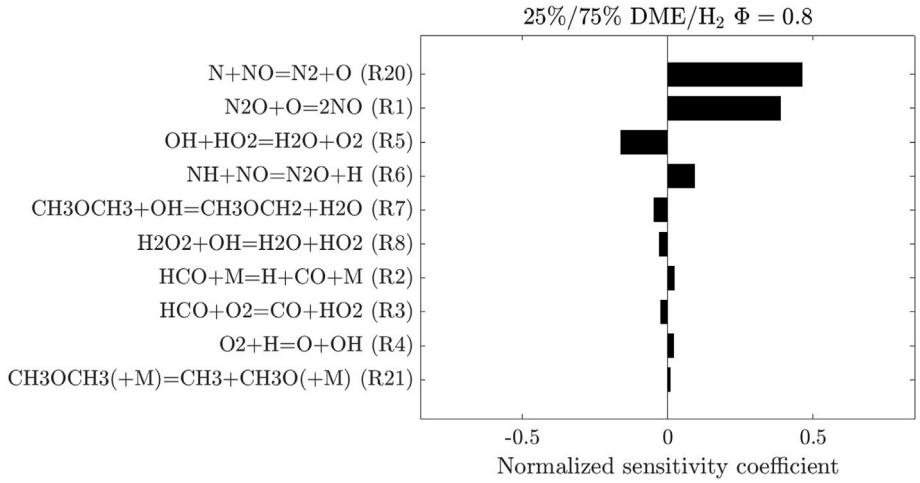

Fig. 30 – Normalised sensitivity coefficients for the 10 most important reactions in NO formation for the 25–75 DME-H_2 mixture at phi = 0.8, performed with the NUIGMech 1.1 mechanism.

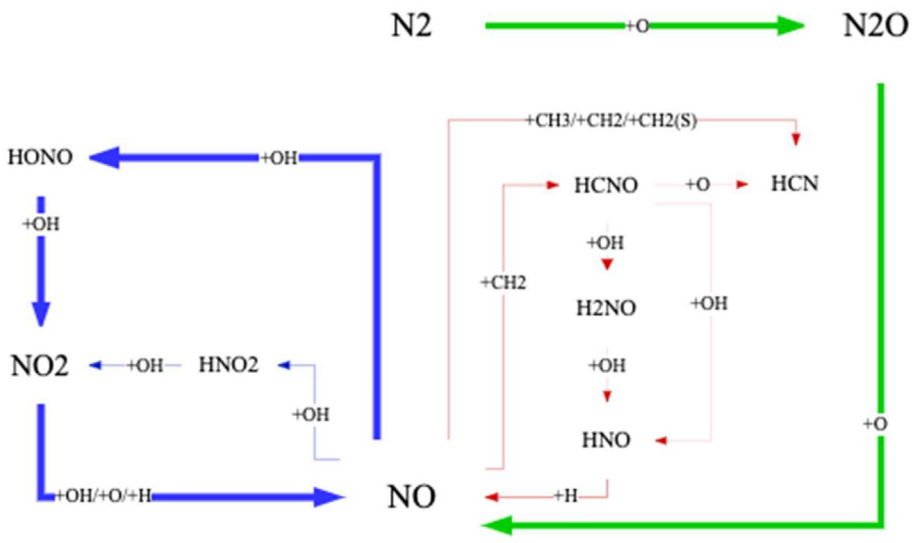

Fig. 31 – Flux analysis of NO formation for the 25–75 DME-CH_4 case at $\Phi = 0.8$ performed with the NUIGMech 1.1 chemical mechanism.

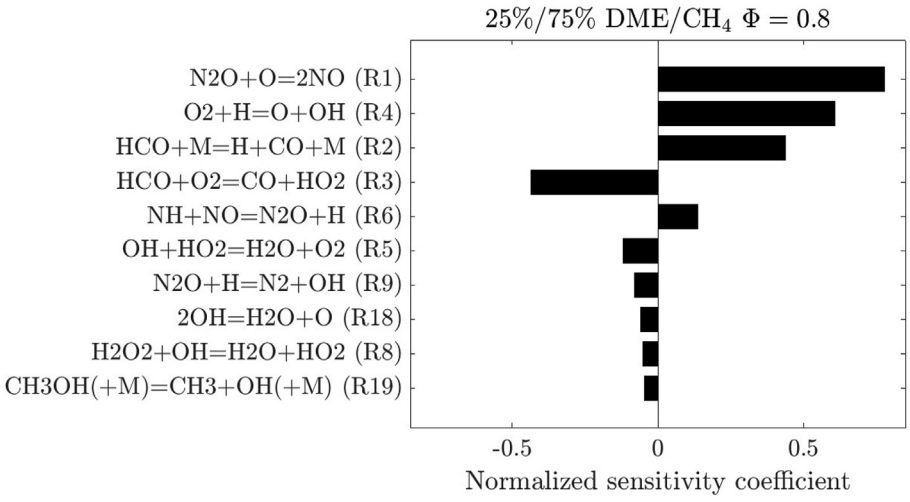

Fig. 32 – Normalised sensitivity coefficients of the 10 most sensitive reactions to NO formation for the 25–75 DME-CH_4 case at $\Phi = 0.8$, performed with the NUIGMech 1.1 chemical mechanism.

Conclusions

The present work investigates the reactive structures and pollutant emissions of dimethyl ether/methane/hydrogen mixtures in a semi-industrial furnace operating with a flameless burner. The potential of partial defossilisation (DME + CH_4) and full defossilisation (DME + H_2) in a flameless capable furnace has been accessed by temperature, chemiluminescence, and species measurements. Further, kinetic analysis based on a simple reactor model has been presented to support the in-depth experimental data. The major findings of the present work are summarised as follows:

(i) Burning dimethyl ether in flameless mode produces ultra-low pollutant emissions in comparison to conventional combustion. For pure DME, a distributed reactive region is stabilised at around 300 mm from the burner exit plane. NO emissions below 10 ppm were observed for all equivalence ratios with no CO and other harmful pollutant emissions.

(ii) The addition of methane into DME resulted in increased ignition delay time and reduced reactivity, thereby creating a favourable environment for the flameless regime. This was confirmed by OH* chemiluminescence and temperature measurements. The reactive region became less intense and moved further downstream (away from the burner) upon CH_4 blending.

(iii) The progressive addition of hydrogen into DME was found to enhance the combustion features. This resulted in the appearance of a visible flame structure characterised by an intense reactive region, higher

peak temperatures, and higher NO emissions. The reactive region for DME/H_2 mixtures formed close to the burner. Kinetic analysis showed that with H_2 addition, the ignition delay times do not vary significantly and rather a combined effect of mixing and the reaction rate dominates in the formation of the reactive region.

(iv) Both peak temperature and NO were lowered upon CH_4 blending. A threshold of 50% CH_4 was defined to achieve net zero NO and CO emissions for all ϕ, thereby suggesting an optimal level of methane blending for practical engineering.

(v) H_2 addition resulted in increased peak temperatures and NO levels. At 50% H_2, CO_2 was reduced by about 18%, and NO stayed around 10 ppm. Maximum measured temperatures were below 1600 K for all equivalence ratios. The burner deviated from flameless features at higher hydrogen content (75% H_2), characterised by increased peak temperatures (1700 K) and NO (about 50 ppm). A threshold of 50% H_2 was found to be optimal for practical engineering.

(vi) The benefit of CO_2 reduction was marginal with methane addition in contrast to hydrogen. For D70M30, D50M50, D40M60, and D25M75, the maximum CO_2 reduction was 9%, 11%, 11.50%, and 14%, respectively. However, it was lowered by 18% and 38% for D50H50 and D25H75, respectively.

(vii) The N_2O pathway was observed to be the root source of NO emissions for pure DME, which is known to play an important role in combustion at lower temperatures [78]. As the equivalence ratio was decreased, the NO formation for pure DME became more sensitive to prompt pathway reactions.

(vii) The addition of methane to pure DME resulted in lower NO emissions due to lower temperatures achieved since the formation pathway of NO did not change substantially. On the other hand, hydrogen addition resulted in increased NO emissions since the thermal pathway became more significant.

(ix) DME and its mixtures with CH_4/H_2 can be potential fuel candidates for use in industrial systems such as steel heat treatment furnaces and glass and ceramic processing plants. These systems are difficult to electrify, and renewable fuels such as DME can completely replace natural gas or propane. As shown in the present work, combustion of DME/CH_4/H_2 mixtures in a flameless capable furnace avoids the temperature peaks and thereby thermal NO. This directly benefits the quality of the charge (steel, glass etc.) and of the furnace material.

Funding

The present work has been funded by i) the European Research Council under the European Union's Horizon 2020 research and innovation programme under grant agreement No. 714605 and ii) the Energy Transition Fund of Belgium.

Declaration of competing interest

The authors declare that they have no known competing financial interests or personal relationships that could have appeared to influence the work reported in this paper.

Acknowledgements

The authors would like to acknowledge the technical support of Marianna Cafiero, Antoine Damilot and Dimitri Iossifidis from the burn laboratory.

Appendix A. Supplementary data

Supplementary data to this article can be found online at https://doi.org/10.1016/j.ijhydene.2022.10.104.

REFERENCES

[1] Park SH, Lee CS. Combustion performance and emission reduction characteristics of automotive DME engine system. Prog Energy Combust Sci 2013;39:147–68.
[2] Zhang W. Automotive fuels from biomass via gasification. Fuel Process Technol 2010;91:866–76.
[3] Semelsberger TA, Borup RL, Greene HL. Dimethyl ether (DME) as an alternative fuel. J Power Sources 2006;156:497–511.
[4] McEnally CS, Pfefferle LD. The effects of dimethyl ether and ethanol on benzene and soot formation in ethylene nonpremixed flames. Proc Combust Inst 2007;31:603–10.
[5] Wook Park S. Numerical study on optimal operating conditions of homogeneous charge compression ignition engines fueled with dimethyl ether and n-heptane. Energy Fuels 2009;23:3909–18.
[6] Teng H, McCandless JC, Schneyer JB. Thermochemical characteristics of dimethyl ether-an alternative fuel for compression-ignition engines. SAE Trans 2001:96–106.
[7] Matteo P, Marta Y, Luis DP, Monica P, Robert E, Laura L. JEC Well-to-Tank report v5. 2020.
[8] Adachi Y, Komoto M, Watanabe I, Ohno Y, Fujimoto K. Effective utilization of remote coal through dimethyl ether synthesis. Fuel 2000;79:229–34.
[9] Liang C, Ji C, Gao B, Liu X, Zhu Y. Investigation on the performance of a spark-ignited ethanol engine with DME enrichment. Energy Convers Manag 2012;58:19–25.
[10] Tang C, Wei L, Zhang J, Man X, Huang Z. Shock tube measurements and kinetic investigation on the ignition delay times of methane/dimethyl ether mixtures. Energy Fuels 2012;26:6720–8.
[11] Chen Z, Qin X, Ju Y, Zhao Z, Chaos M, Dryer FL. High temperature ignition and combustion enhancement by dimethyl ether addition to methane-air mixtures. Proc Combust Inst 2007;31:1215–22.
[12] Burke U, Somers KP, O'Toole P, Zinner CM, Marquet N, Bourque G, et al. An ignition delay and kinetic modeling study of methane, dimethyl ether, and their mixtures at high pressures. Combust Flame 2015;162:315–30.
[13] Song J, Huang Z, Qiao X, Wang W. Performance of a controllable premixed combustion engine fueled with dimethyl ether. Energy Convers Manag 2004;45:2223–32.

[14] Park SH, Lee CS. Applicability of dimethyl ether (DME) in a compression ignition engine as an alternative fuel. Energy Convers Manag 2014;86:848–63.
[15] Kim MY, Yoon SH, Ryu BW, Lee CS. Combustion and emission characteristics of DME as an alternative fuel for compression ignition engines with a high pressure injection system. Fuel 2008;87:2779–86.
[16] Lu X, Han D, Huang Z. Fuel design and management for the control of advanced compression-ignition combustion modes. Prog Energy Combust Sci 2011;37:741–83.
[17] Jin T, Wu Y, Wang X, Luo KH, Lu T, Luo K, et al. Ignition dynamics of DME/methane-air reactive mixing layer under reactivity controlled compression ignition conditions: effects of cool flames. Appl Energy 2019;249:343–54.
[18] Desai S, Sankaran R, Im HG. Auto-ignitive deflagration speed of methane (CH4) blended dimethyl-ether (DME)/air mixtures at stratified conditions. Combust Flame 2020;211:377–91.
[19] Anggarani R, Wibowo CS, Rulianto D. Application of dimethyl ether as LPG substitution for household stove. Energy Proc 2014;47:227–34.
[20] Larson ED, Yang H. Dimethyl ether (DME) from coal as a household cooking fuel in China. Energy for sustainable development 2004;8:115–26.
[21] Panigrahy S, Mishra SC. The combustion characteristics and performance evaluation of DME (dimethyl ether) as an alternative fuel in a two-section porous burner for domestic cooking application. Energy 2018;150:176–89.
[22] Arya P, Tupkari S, Satish K, Thakre G, Shukla B. DME blended LPG as a cooking fuel option for Indian household: a review. Renew Sustain Energy Rev 2016;53:1591–601.
[23] Marchionna M, Patrini R, Sanfilippo D, Migliavacca G. Fundamental investigations on di-methyl ether (DME) as LPG substitute or make-up for domestic uses. Fuel Process Technol 2008;89:1255–61.
[24] Grové J. Energy transitions in developing countries and the role of alternative liquid fuels in reducing energy poverty: exploring the use of domestically produced dimethyl ether (DME) to augment the use of imported liquefied petroleum gas (LPG) as a clean cooking fuel in India. 2018.
[25] Lee MC, Seo SB, Chung JH, Joo YJ, Ahn DH. Industrial gas turbine combustion performance test of DME to use as an alternative fuel for power generation. Fuel 2009;88:657–62.
[26] Gupta KK, Rehman A, Sarviya R. Bio-fuels for the gas turbine: a review. Renew Sustain Energy Rev 2010;14:2946–55.
[27] Gökalp I, Lebas E. Alternative fuels for industrial gas turbines (AFTUR). Appl Therm Eng 2004;24:1655–63.
[28] Lee MC, Yoon Y. Development of a gas turbine fuel nozzle for DME and a design method thereof. Fuel 2012;102:823–30.
[29] Jiang L, Zhao D, Guo C, Wang X. Experimental study of a plat-flame micro combustor burning DME for thermoelectric power generation. Energy Convers Manag 2011;52:596–602.
[30] Seo SH, Lee CS. Effects of dimethyl ether on the performance characteristics of a direct methanol fuel cell. Energy Convers Manag 2013;70:239–43.
[31] Chen R, Wang H-t, Wang H. Different oxygen levels of dimethyl ether combustion influence numerical simulation. Procedia Eng 2012;31:934–40.
[32] Kang Y, Lu X, Wang Q, Ji X, Miao S, Xu J, et al. Experimental and modeling study on the flame structure and reaction zone size of dimethyl ether/air premixed flame in an industrial boiler furnace. Energy Fuels 2013;27:7054–66.
[33] Kang Y, Lu X, Wang Q, Ji X, Miao S, Zong C, et al. An experimental and modeling study of NOx and CO emission behaviors of dimethyl ether (DME) in a boiler furnace. Fuel Process Technol 2014;122:129–40.
[34] Kang Y, Wang Q, Lu X, Wan H, Ji X, Wang H, et al. Experimental and numerical study on NOx and CO emission characteristics of dimethyl ether/air jet diffusion flame. Appl Energy 2015;149:204–24.
[35] Wang Y, Liu H, Ke X, Shen Z. Kinetic modeling study of homogeneous ignition of dimethyl ether/hydrogen and dimethyl ether/methane. Appl Therm Eng 2017;119:373–86.
[36] Kang Y, Lu X, Wang Q, Gan L, Ji X, Wang H, et al. Effect of H2 addition on combustion characteristics of dimethyl ether jet diffusion flame. Energy Convers Manag 2015;89:735–48.
[37] Kang Y, Shuang W, Jiang X, Song Y, Sun S, Zhang P, et al. Study on effect of dimethyl ether addition on combustion characteristics of turbulent methane/air jet diffusion flame. Fuel Process Technol 2017;159:421–35.
[38] Bhattacharya A, Basu S. An investigation into the heat release and emissions from counterflow diffusion flames of methane/dimethyl ether/hydrogen blends in air. Int J Hydrogen Energy 2019;44:22328–46.
[39] Pan L, Hu E, Deng F, Zhang Z, Huang Z. Effect of pressure and equivalence ratio on the ignition characteristics of dimethyl ether-hydrogen mixtures. Int J Hydrogen Energy 2014;39:19212–23.
[40] Liu J, Wang H, Ouyang M. Kinetic modeling study of hydrogen addition to premixed dimethyl ether-oxygen-argon flames. Int J Hydrogen Energy 2011;36:15860–7.
[41] Lowry W, Serinyel Z, Krejci M, Curran H, Bourque G, Petersen E. Effect of methane-dimethyl ether fuel blends on flame stability, laminar flame speed, and Markstein length. Proc Combust Inst 2011;33:929–37.
[42] Yu H, Hu E, Cheng Y, Yang K, Zhang X, Huang Z. Effects of hydrogen addition on the laminar flame speed and markstein length of premixed dimethyl ether-air flames. Energy Fuels 2015;29:4567–75.
[43] OoI Technologies. Combustion - research and development. United States: Office of Energy Efficiency and Renewable Energy U.S. Department of Energy; 2001.
[44] Wünning J, Wünning J. Flameless oxidation to reduce thermal NO-formation. Prog Energy Combust Sci 1997;23:81–94.
[45] Cavaliere A, De Joannon M. Mild combustion. Prog Energy Combust Sci 2004;30:329–66.
[46] Katsuki M, Hasegawa T. The science and technology of combustion in highly preheated air. In: Symposium (international) on combustion. Elsevier; 1998. p. 3135–46.
[47] Arghode VK, Gupta AK. Effect of flow field for colorless distributed combustion (CDC) for gas turbine combustion. Appl Energy 2010;87:1631–40.
[48] Lückerath R, Meier W, Aigner M. FLOX® combustion at high pressure with different fuel compositions. J Eng Gas Turbines Power 2008;130.
[49] Mi J, Li P, Dally BB, Craig RA. Importance of initial momentum rate and air-fuel premixing on moderate or intense low oxygen dilution (MILD) combustion in a recuperative furnace. Energy Fuels 2009;23:5349–56.
[50] Szego GG. Experimental and numerical investigation of a parallel jet MILD combustion burner system in a laboratory-scale furnace. 2010.
[51] Tsuji H, Gupta AK, Hasegawa T, Katsuki M, Kishimoto K, Morita M. High temperature air combustion: from energy conservation to pollution reduction. CRC press; 2002.
[52] Kumar S, Paul P, Mukunda H. Investigations of the scaling criteria for a mild combustion burner. Proc Combust Inst 2005;30:2613–21.
[53] Sharma S, Singh P, Gupta A, Chowdhury A, Khandelwal B, Kumar S. Distributed combustion mode in a can-type gas turbine combustor-A numerical and experimental study. Appl Energy 2020;277:115573.
[54] Sharma S, Pingulkar H, Chowdhury A, Kumar S. A new emission reduction approach in MILD combustion through asymmetric fuel injection. Combust Flame 2018;193:61–75.

[55] Sharma S, Chowdhury A, Kumar S. A novel air injection scheme to achieve MILD combustion in a can-type gas turbine combustor. Energy 2020;194:116819.
[56] Ardila FEC, Arbeláez JEO, Arrieta AAA. Emissions and dynamic stability of the flameless combustion regime using hydrogen blends with natural gas. Int J Hydrogen Energy 2021;46:1246–58.
[57] Colorado A, Herrera B, Amell A. Performance of a flameless combustion furnace using biogas and natural gas. Bioresour Technol 2010;101:2443–9.
[58] Derudi M, Villani A, Rota R. Mild combustion of industrial hydrogen-containing byproducts. Ind Eng Chem Res 2007;46:6806–11.
[59] Hosseini SE, Wahid MA. Biogas utilization: experimental investigation on biogas flameless combustion in lab-scale furnace. Energy Convers Manag 2013;74:426–32.
[60] Huang M, Zhang Z, Shao W, Xiong Y, Liu Y, Lei F, et al. Effect of air preheat temperature on the MILD combustion of syngas. Energy Convers Manag 2014;86:356–64.
[61] Zhao Y, McDonell V, Samuelsen S. Assessment of the combustion performance of a room furnace operating on pipeline natural gas mixed with simulated biogas or hydrogen. Int J Hydrogen Energy 2020;45:11368–79.
[62] Ayoub M, Rottier C, Carpentier S, Villermaux C, Boukhalfa A, Honoré D. An experimental study of mild flameless combustion of methane/hydrogen mixtures. Int J Hydrogen Energy 2012;37:6912–21.
[63] Chinnici A, Nathan G, Dally B. Combined solar energy and combustion of hydrogen-based fuels under MILD conditions. Int J Hydrogen Energy 2018;43:20086–100.
[64] Mardani A, Mahalegi HKM. Hydrogen enrichment of methane and syngas for MILD combustion. Int J Hydrogen Energy 2019;44:9423–37.
[65] Hosseini SE, Bagheri G, Wahid MA. Numerical investigation of biogas flameless combustion. Energy Convers Manag 2014;81:41–50.
[66] Ferrarotti M, De Paepe W, Parente A. Reactive structures and NOx emissions of methane/hydrogen mixtures in flameless combustion. Int J Hydrogen Energy 2021;46:34018–45.
[67] Sorrentino G, Sabia P, Bozza P, Ragucci R, de Joannon M. Low-NOx conversion of pure ammonia in a cyclonic burner under locally diluted and preheated conditions. Appl Energy 2019;254:113676.
[68] Kang Y, Lu T, Lu X, Wang Q, Huang X, Peng S, et al. Study on combustion characteristics of dimethyl ether under the moderate or intense low-oxygen dilution condition. Energy Convers Manag 2016;108:549–65.
[69] Kang Y, Wei S, Zhang P, Lu X, Wang Q, Gou X, et al. Detailed multi-dimensional study on NOx formation and destruction mechanisms in dimethyl ether/air diffusion flame under the moderate or intense low-oxygen dilution (MILD) condition. Energy 2017;119:1195–211.
[70] Ferrarotti M, Fürst M, Cresci E, De Paepe W, Parente A. Key modeling aspects in the simulation of a quasi-industrial 20 kW moderate or intense low-oxygen dilution combustion chamber. Energy Fuels 2018;32:10228–41.
[71] Varghese RJ, Kolekar H, Kishore VR, Kumar S. Measurement of laminar burning velocities of methane-air mixtures simultaneously at elevated pressures and elevated temperatures. Fuel 2019;257:116120.
[72] Tayur Nagendra V, Parameshwara V. Numerical study of autoignition of fuel-air mixtures at elevated temperatures and pressures. 2021.
[73] Mohamed AAE-S, Panigrahy S, Sahu AB, Bourque G, Curran HJ. An experimental and kinetic modeling study of the auto-ignition of natural gas blends containing C1-C7 alkanes. Proc Combust Inst 2021;38:365–73.
[74] Galletti C, Parente A, Derudi M, Rota R, Tognotti L. Numerical and experimental analysis of NO emissions from a lab-scale burner fed with hydrogen-enriched fuels and operating in MILD combustion. Int J Hydrogen Energy 2009;34:8339–51.
[75] Li P, Wang F, Mi J, Dally B, Mei Z, Zhang J, et al. Mechanisms of NO formation in MILD combustion of CH4/H2 fuel blends. Int J Hydrogen Energy 2014;39:19187–203.
[76] Parente A, Galletti C, Tognotti L. Effect of the combustion model and kinetic mechanism on the MILD combustion in an industrial burner fed with hydrogen enriched fuels. Int J Hydrogen Energy 2008;33:7553–64.
[77] http://creckmodeling.chem.polimi.it/menu-kinetics/menu-kinetics-detailed-mechanisms. 2022.
[78] Glarborg P, Miller JA, Ruscic B, Klippenstein SJ. Modeling nitrogen chemistry in combustion. Prog Energy Combust Sci 2018;67:31–68.